MULTIPLEXED ELECTROSPRAY EMITTERS

FOR HIGHLY CONDUCTIVE AND CORROSIVE FLUIDS

LIURUI LI

Thesis submitted to the faculty of the
Virginia Polytechnic Institute and State University
in partial fulfillment of the requirements for the degree of

Master of Science
In
Mechanical Engineering

Weiwei Deng
Yang Liu
Jiangtao Cheng

April 27, 2017
Blacksburg, VA

Keywords: Electrospray, Multiplexed electrospray emitter, Thin-film deposition

MULTIPLEXED ELECTROSPRAY EMITTERS

FOR HIGHLY CONDUCTIVE AND CORROSIVE FLUID

Liurui Li

ABSTRACT

Liquid sprays have widespread applications such as spray coating, spray drying, spray pyrolysis, and spray cooling. Among various types of sprays, electrohydrodynamic spray (electrospray) has several unique properties such as quasi-monodispersity, tunable droplet size from a few micrometer to nanometers, and compatible with roll-to-roll processing of advanced materials. On the other hand, solution-processed perovskite solar cells have attracted immense research interest recently: within the past seven years, efficiencies of perovskite solar cells have rapidly increased from 3.8% to over 20%. Electrospray is a potential film deposition technique to replace spin coating for continuously fabricating thin-film perovskite solar cells with large areas and virtually no material waste. However, two major challenges exist for electrospraying liquid solutions of perovskite precursors. First, the solution is highly corrosive due to lead (Pb) ions which prevent the use of common metals (i.e. copper, stainless steel, and aluminum). Second, the solution is highly electrical conductive which demands low flow rates (~100nL/min) which make it difficult to multiplex. This thesis reports the design, fabrication, and operation of silicone based multiplexed electrospray (MES) emitters. After reviewing the feasibility of utilizing electrospray as a scalable thin film deposition technique as well as the advantages and limitations of prior MES emitters, we present a design rationale for MES suitable for highly conductive and corrosive fluids. Then we customized a 1064nm fiber laser micromachining system to precisely and rapidly machine silicone sheet and silicon wafers. Laser energy and path are judicially chosen to create clean and round micro posts that form the external structure of the nozzles. For MES with low flow rate per nozzle, it is of vital importance to evenly distribute the liquid into each nozzle on the entire MES array by controlling the pressure drop inside each fluid flow channel. To this end, we modeled the dimension of microfluidic channels

that introduce flow impedance overwhelming surface tension at the nozzle tip. We presented laser microfabrication techniques for fabricating two typical types of microfluidic channels: the through-hole array on conductive silicone sheets and the in-plane microfluidic channel on silicon wafers. Next, we developed a convenient assemble process for the integration of three layers (distributor layer, extractor layer, and collector layer) of the MES emitter. The uniformity of the flow rate among nozzles on MES emitters was investigated by observing the overall spray profiles and measuring the diameter of each jet. The results suggest that the silicone-based MES emitters are feasible for spraying highly conductive and corrosive liquids. The MES emitter developed in this thesis may become a promising tool in scalable manufacturing of thin film perovskite solar cells.

MULTIPLEXED ELECTROSPRAY EMITTERS

FOR HIGHLY CONDUCTIVE AND CORROSIVE FLUID

Liurui Li

GENERAL AUDIENCE ABSTRACT

Liquid sprays have widespread applications such as spray coating, spray drying, spray pyrolysis, and spray cooling. Among various types of sprays, electrohydrodynamic spray (electrospray) has several unique properties such as quasi-monodispersity, tunable droplet size from a few micrometer to nanometers, and compatible with roll-to-roll processing of advanced materials. On the other hand, solution-processed perovskite solar cells have attracted immense research interest recently: within the past seven years, efficiencies of perovskite solar cells have rapidly increased from 3.8% to over 20%. Electrospray is a potential film deposition technique to replace spin coating for continuously fabricating thin-film perovskite solar cells with large areas and virtually no material waste. However, two major challenges exist for electrospraying liquid solutions of perovskite precursors. First, the solution is highly corrosive due to lead (Pb) ions which prevent the use of common metals (i.e. copper, stainless steel, and aluminum). Second, the solution is highly electrical conductive which demands low flow rates (~100nL/min) which make it difficult to multiplex. This thesis reports the design, fabrication, and operation of silicone based multiplexed electrospray (MES) emitters. After reviewing the feasibility of utilizing electrospray as a scalable thin film deposition technique as well as the advantages and limitations of prior MES emitters, we present a design rationale for MES suitable for highly conductive and corrosive fluids. Then we customized a 1064nm fiber laser micromachining system to precisely and rapidly machine silicone sheet and silicon wafers. Laser energy and path are judicially chosen to create clean and round micro posts that form the external structure of the nozzles. For MES with low flow rate per nozzle, it is of vital importance to evenly distribute the liquid into each nozzle on the entire MES array by controlling the pressure drop inside each fluid flow channel. To this end, we modeled the dimension of microfluidic channels that introduce flow impedance overwhelming surface tension at the nozzle tip. We presented

laser microfabrication techniques for fabricating two typical types of microfluidic channels: the through-hole array on conductive silicone sheets and the in-plane microfluidic channel on silicon wafers. Next, we developed a convenient assemble process for the integration of three layers (distributor layer, extractor layer, and collector layer) of the MES emitter. The uniformity of the flow rate among nozzles on MES emitters was investigated by observing the overall spray profiles and measuring the diameter of each jet. The results suggest that the silicone-based MES emitters are feasible for spraying highly conductive and corrosive liquids. The MES emitter developed in this thesis may become a promising tool in scalable manufacturing of thin film perovskite solar cells.

ACKNOWLEDGEMENTS

Dr. Weiwei Deng has been not only an incredible research advisor, but also an amazing mentor for me in the past two years. I started from scratch in the field of microfluidics when I became a member of the Deng Lab. It was his patient guidance that led me through those hard days. His passion towards science also encouraged me to keep digging my potential. All in all, it has been a great honor to be instructed by Dr.Weiwei Deng. I also thank Drs Yang Liu and Jiangtao Cheng for serving in my thesis committee.

I have to thank my lab mate Fan Gao, who is also my close friend. He helped me a lot on both programming and using engineering software.

I must thank Ting Yang who is the most diligent student I ever worked with. She kindly offered me assistances whenever I met problems on theoretical derivation related to my research works and courses.

Special thanks to my lab mate Yuanyuan Jiang who has been my on-call material science expert. This thesis could not have been accomplished without her dedicated help.

I express my deepest gratitude to my parents who always support my right decisions and correct my naive illusions in the past 24 years. I am fortunate to have them in my life.

TABLE OF CONTENTS

CHAPTER 1: INTRODUCTION 1

1.1 Electrospray as a scalable thin film deposition technique 2

1.2 State of art of multiplexed electrospray 3

1.2.1 Conventional techniques 4

1.2.2 Emerging techniques for MES device fabrication 6

1.3 Deposition of thin film Perovskite: an example of highly corrosive and conducting liquid in need of MES 8

1.3.1 Perovskite semiconductor and its excellent properties 9

1.3.2 The need an feasibility of creating perovskite thin films by electrospray 11

1.4 Thesis overview 14

CHAPTER 2: Laser micromachining of nozzle external structure 16

2.1 Machine tool 16

2.1.1 Principles 17

2.1.2 System Modification 18

2.1.3 Process Parameters 18

2.2 External structure milling 19

2.2.1 Surface topography 20

2.2.2 Laser beam scanning strategy 22

2.2.3 Power level 23

2.2.4 Post cleaning process 24

Chapter 3 Laser Machining of Channels with High Flow Impedance 25

3.1 Through hole drilling 25

3.1.1 Through hole flow resistance 26
3.1.2 Drilling parameters 27
3.1.3 Finish circularity 29
3.1.4 Inner wall quality 29
3.1.5 Through-hole array uniformity 30
3.2 Microfluidic channel 31
3.2.1 Microfluidic channel flow resistance 32
3.2.2 Systematic test of single laser spot 32
3.2.3 Configuration of flow-resistive channels 35
Chapter 4 System design and implementation 36
4.1 Design of Electrodes 37
4.1.1 Distributor 37
4.1.2 Extractor 39
4.1.3 Collector 40
4.2 System Integration 40
4.2.1 Reservoir sealing 40
4.2.2 Electrical connection and insulation 41
4.2.3 Liquid supply 42
CHAPTER 5: MES emitters operation 43
5.1 Estimation of critical field 43
5.2 Spray profile 44
5.3 Flow rate uniformity 46
CHAPTER 6: CONCLUSIONS 48
LIST OF REFERENCE 49

LIST OF FIGURES

Figure 1: (a) typical electrospray; (b) details of the jet break-up 3
Figure 2: Image of brute force MES emitters: (a) Rulison and Flagan 1993; (b) Kelly et al 2008 4
Figure 3: Image of silicon microfabrication MES emitters: (a) Planar nozzle array and corresponding (b) MES spray profiles [3]; (c) Planar nozzle array and flow-resistive channels [10] 5
Figure 4：Linear MES arrays machined in brass (top), aluminum (center), and polycarbonate (bottom) 6
Figure 5: Image of additive manufactured MES emitters: (a),(b) polymer MES emitters; (c) coaxial MES emitter 7
Figure 6: (a) SEM images of an emitter that is part of a sparse emitter array, along with close-up images of the CNTs grown on the emitter surface; (b) SEM images of a dense array of emitters coated with CNTs, along with close-up images of a single emitter and emitter tip. [12] 8
Figure 7: The graph shows a meteoric rise compared to most other technologies over a relatively short period of time. In the space of three years, perovskite solar cells have managed to achieve power conversion efficiencies comparable to Cadmium Telluride, which has been around for nearly 40 years. 9
Figure 8: (a) Perovskite structure [14] (b) Classic DSSC with complex nano/meso structure of ~10 μm in thickness [15] (c) Planar perovskite device (side view) [16] 9
Figure 9 : (a) Experimental setup for ES processing of perovskite film. (b) The Taylor cone, which is visualized by a long working distance microscope objective lens coupled with a Canon 650D camera. The resolving power is 1 μm/pixel. The jet is too small to resolve. (Unpublished results) 12

Figure 10 : Solid film of electrospray deposited perovskite (a) Optical image, the half circle at the top is where the ES started; (b) Scanning electronic microgram (SEM), with dark color as ruptured area; and (c) X-ray diffraction (XRD). Unpublished results. 14
Figure 11 Modified 10W RGL-FM Fiber Laser Marker 18
Figure 12：Laser milled conductive sealing part (left) and the original rubber part (right) 20
Figure 13 : Illustration of the step, pulse overlap and step overlap [30] 21
Figure 14: Surface topography of milled surface machined under (a) high step with high scan speed; (b) high step with low scan speed; (c) low step with high speed; (d) low step with low speed 21
Figure 15: (a) Circular scan path, (b) spiral scan path.....22
Figure 16: Top view of nozzles machined with: (a) (b) circular path; (c) spiral path.....23
Figure 17: Dummy nozzles machined under (a) 100% power; (b) 50% power; (c) 2% power23
Figure 18: 300 μm nozzle top finish (a) right after the milling; (b) after ultrasonic cleaning; (c) after lens wiper cleaning.....24
Figure 19: 18×18 dummy nozzle array.....24
Figure 20: Surface topography of laser affected area 28
Figure 21: Through hole exit with (a) 55 μm diameter; (b) 30 μm diameter; (c) 20 μm diameter 28
Figure 22: Through hole entry without (a), with (b) sacrifice layer; through hole exit without (c), with (d) sacrifice layer.....29
Figure 23: Inner wall topography of the laser drilled through hole.....30
Figure 24: Nozzle array cutter.....31
Figure 25: Samples for studying the contribution of power level and workpiece location 33
Figure 26: Material removal of single laser pulse at the focus 33
Figure 27: Cross-section of single pits under machined with different power level.....34
Figure 28: Surface topography of single laser spots.....35
Figure 29: Microfluidic channels on silicon wafer.....35
Figure 30: Diagram for the typical three-electrode MES emitter[11].....36
Figure 31:（a）16×16 square nozzle array surrounded by dummy nozzles: (b) SEM scan of a single nozzle. Image was taken at 45° angle with respect to the surface normal.....38

Figure 32 ： 12×1 linear nozzle array with (a) 150 μm OD, 1mm pitch; (b) 175 μm OD, 1 mm pitch; (c) 16×1 linear nozzle array with 300 μm OD, 0.75 mm pitch.....39
Figure 33: Extractor machined on stainless steel with a 500 μm slot 39
Figure 34：Nozzle array with ID=55, OD=150, P=1mm, N=10: (a) stable cone jets, (c)spray profiles; Nozzle array with ID=55, OD=175, P=1mm, N=10: (a) stable cone jets, (b)spray profiles; (e)spray profiles of a nozzle array with ID=55, OD=150, P=1mm, N=16.....45
Figure 35: Stable cone jets of a 16×1 nozzle array under Q=1.2ml/h/nozzle 47
Figure 36: The cone-jet diameter of a 16×1 nozzle array under different flow rate 47

LIST OF TABLES

Table 1: Characteristics summary of conventional MES emitters 6
Table 2: Characteristic summary of additive manufacturing MES approaches 7
Table 3: Comparison between perovskite and other solution processable photovoltaics [19-24] 11
Table 4: Parameters of modified the RGL-FM fiber laser marker 19
Table 5: Milling parameters for nozzles with 300 μm OD 23
Table 6: System parameters for through hole drilling 28
Table 7: Average inner diameter of nozzles at different depth of the material 31
Table 8: Volume of silicon removed by a single laser pulse 34
Table 9: Diameter uniformity of jets right above the extractor 47

CHAPTER 1: INTRODUCTION

Electrohydrodynamic spray, or more generally electrospray, is a liquid atomization technique that can generate fine droplets with high degree of uniformity. By supplying the liquid with sufficient conductivity to a capillary, a single spray can form between the capillary charged at high electric potentials and a nearby-grounded substrate. At the tip of the capillary, liquid meniscus can form four typical modes of operation: dripping mode, cone-jet mode, microdripping mode and spindle mode [1]. Among these modes, the most well-known and widely applicable mode is the cone-jet mode, also known as Tayler-cone for Taylor was the first to demonstrate that surface tension and electric stress can be balanced at any point on a liquid cone surface [2]. Influenced by Rayleigh instability, jets emanate from the conical form at the capillary tip will break up into two types of droplets: the primary droplets and satellite droplets. The primary droplet will domain the mass and the charge when forming the core of the spray region while the satellite droplet will form the shroud due to their small inertia and strong initial repulsions.

The unique advantage of electrospray compared to many other atomization techniques is that the diameter of droplets inside the self-dispersion spray can be easily controlled by electric charge level, flow rate, conductivity of the liquid and the geometry of the capillary, which results in a flexible droplet dimension from nanometers to micrometers with excellent size uniformity. Such properties enable the electrospray to find numerous applications in the field of biotechnology and nanotechnology, among which the most famous example is Electrospray Ionization Mass Spectrometry (ESI-MS). ESI-MS was first introduced by Masamichi Yamashita and John Fenn in1984, the later was rewarded with the Nobel Prize in Chemistry in 2002 for using electrospray to introduce in the gas phase multiply charged macromolecule ions, originally in solution, for subsequent analysis in a mass spectrometer [3].

However, one obstacle that prevents the electrospray technique from being used at the industrial level is that the optimum flow rate for a single capillary electrospray system is extremely low, usually on the order of milliliters per hour. To achieve practical goals such as mass production of drug carrier, thrusters for aerospace propulsion or roll-to-toll deposition of

thin films, the electrospray system must be scaled up or multiplexed. Multiplexed electrospray (MES) devices have been designed and implemented since 90's[4]. Besides the difficulty in manufacturing the nozzle array with proper material and machine process, it is also challenging to fully understand the intricate interaction between nozzles and sprays when operating a large number of nozzles simultaneously. A reliable MES system is of vital importance for scaling up the total flow rate and increase the efficiency of this technique aiming at industrial applications.

1.1 Electrospray as a scalable thin film deposition technique

Our research lab is interested in the use of electrospray (ES) as the deposition technique for making thin liquid films primarily because ES has the unmatched capability of producing uniform droplets in the sub-1 μm range. Based on a typical thin film of perovskite (to be discussed in details in Section 1.3), the targeted dry film thickness of ~300 nm and 10 vol% concentration, the initial liquid film thickness needs only to be ~3 μm. To create a uniform liquid film by droplet deposition, the droplet diameter should be well below 3 μm, and preferably less than 1 μm. Other roll-to-roll compatible methods such as ink jet [5], screen printing [6], doctor blading [7], and pneumatic spray coatin [8] are in principle not suitable for perovskite because the thickness of dried films made by those methods are well over 300 nm, unless very dilute (1 vol% or less) solution is used.

A typical ES system (Figure 1 a) can be implemented by feeding a liquid with sufficient electrical conductivity through a small capillary that is charged to a few kV relative to a nearby ground electrode. The liquid forms on a conical shape (termed Taylor-cone) resulting from the balance of surface tension and electric normal stress. The electric shear stress drives the liquid near the free liquid surface, and accelerates the liquid into a fine jet issuing from the cone. This unique draw-down jetting mechanism eliminates liquid-solid friction, which enables ES to generate droplet hundreds of times smaller than the nozzle opening with little risk of clogging.

The droplet diameter can be estimated by scaling laws , and for highly conducting liquid the scaling laws state $d \propto (Q/k)^{1/3}$, where d is the droplet diameter, k the liquid electrical conductivity, and Q the liquid flow rate. The scaling law suggests that liquids with high k, such as the salt solution used in this research, can produce sub-micrometer droplets. The fine control

of droplet diameter through flow rate Q enables us to strike a good balance between small building block size and sufficient throughput.

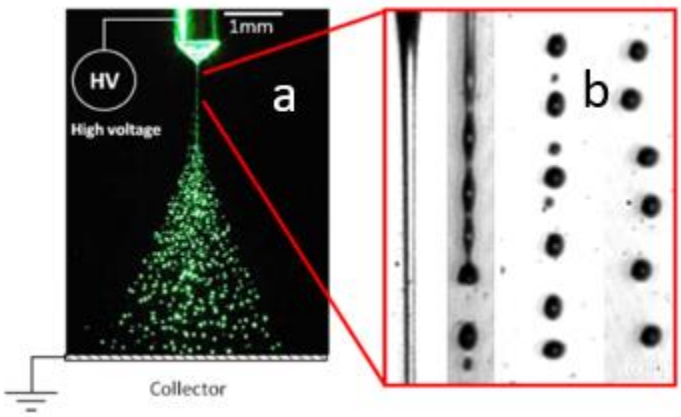

Figure 1: (a) typical electrospray; (b) details of the jet break-up

1.2 State of art of multiplexed electrospray

The very first MES system was developed by Snarski and Dunn in 1991 to study the interaction between two electrosprays with two electrodes (emitter and collector). To operating the MES system with high nozzle density, three-electrodes design (distributor, extractor, and collector) were designed and successfully implemented. This configuration divided the spray area into two regions: the cone-jet region and the spray forming region, which will be discussed in detail in Chapter 4.

MES systems developed previously vary in nozzle materials and nozzle array configurations due to their respective applications. Polymers, silicon, stainless steel, fused silica, PDMS, and polycarbonate are all potential nozzle materials when utilizing proper machine processes which may impose restrictions on the configuration of nozzles and nozzle arrays. Conventionally, nozzle arrays in a MES systems were mainly manufactured by the following three methods: brute force, silicon microfabrication and subtractive manufacturing. Recently, a

few newly fabrication methods have emerged and contributed to the "toolbox" for creating MES emitters.

1.2.1 Conventional techniques

Brute force, silicon microfabrication and subtractive manufacturing are three typical techniques for the realization of the MES nozzle array's configuration. A brief summary of nozzle arrays' parameters machined with techniques mentions above is shown in Table 1.

The concept of brute force techniques is to simply assemble several individual needles onto a common base and supply liquids either individually or using a common reservoir. As the earliest version of the MES technique, brute force MES devices utilized stainless steel with the inner diameter more than 200 microns. Despite the simple concept of the brute force technique, the maximum number of nozzles that can be integrated was less than other techniques. Kelly and co-workers [9] published a silica based brute force MES system with a nozzle array consists of 19 individual nozzles.

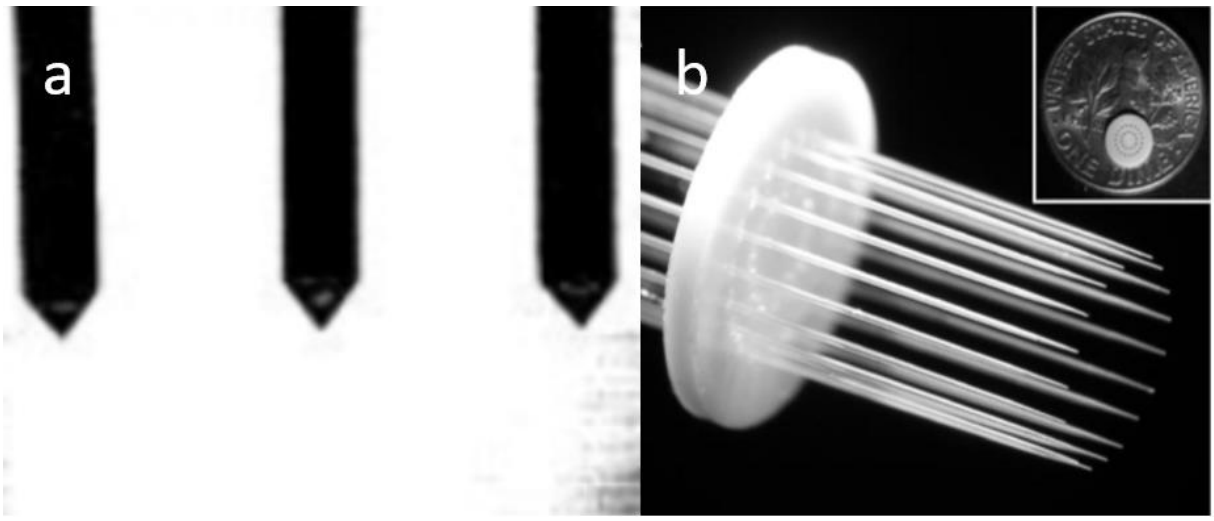

Figure 2: Image of brute force MES emitters: (a) Rulison and Flagan 1993; (b) Kelly et al 2008

Silicon microfabrication of MES nozzle arrays uses photolithography to precisely define the nozzle geometry with masks and chemical etching of the silicon wafer. Both advantages and disadvantages of this technique are apparent. Similar to stereolithography process in 3-D printing, the redundant material is removed layer by layer, which enables this technique to produce a large number of nozzles simultaneously in a restricted area which resulted in a

packing density of 11,547sources/cm^2 reported by Deng et al [3]. Grustan -Gutierrez and Gamero-Castaño successfully integrated the flow resistive liquid supply channels on one side of silicon wafer while the nozzle array was etched on the other side of the silicon wafer [10]. Despite the existence of numerous advantages of a micro-fabricated silicon emitter, this technique is still not applicable in an industrial level. The complexity of the whole fabrication process and the high fixed cost make it not suitable for rapid prototyping. In addition, this method limits the nozzle material to silicon, which is brittle and does not offer sufficient mechanical strength for small nozzles with high aspect ratios.

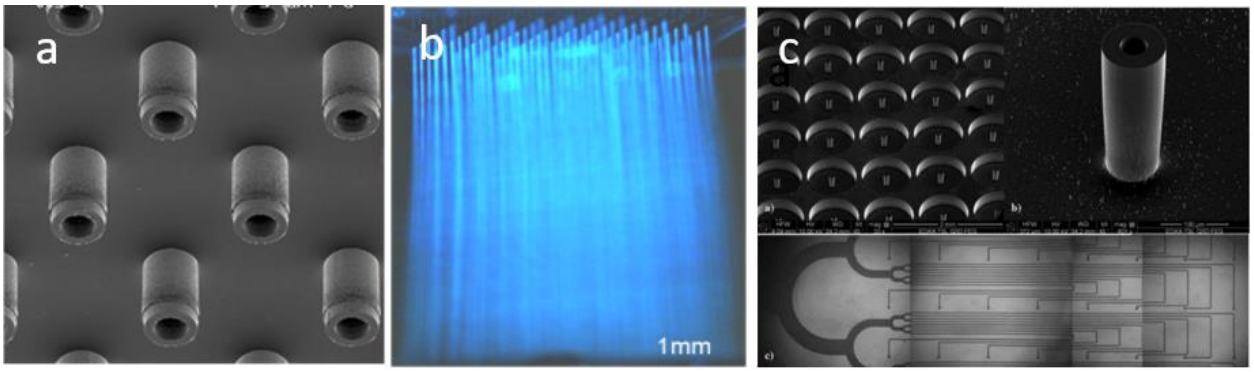

Figure 3: Image of silicon microfabrication MES emitters: (a) Planar nozzle array and corresponding (b) MES spray profiles [3]; (c) Planar nozzle array and flow-resistive channels [10]

Subtractive manufacturing is the technique with the flexibility for implementing design changes. Computer Aid Design (CAD) enables us to conveniently control the path of the machine tool, either cutting tools or laser, enabling us to machine varies micro-structures on numerous materials. For example, the inner diameter of the nozzle machined by micro drilling could reach as small as 50 microns [11] in brass, aluminum, and polycarbonate (Figure 4).

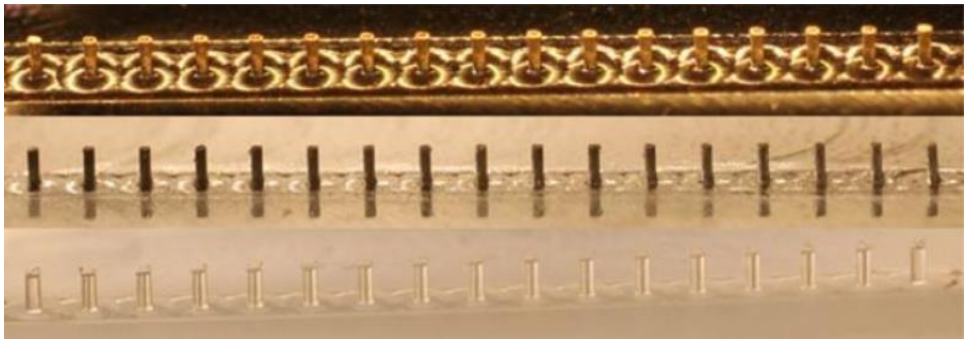

Figure 4 : Linear MES arrays machined in brass (top), aluminum (center), and polycarbonate (bottom)

Table 1: Characteristics summary of conventional MES emitters

Technique	Year	Author	Configuration	Nozzle material	n	P	ID	L
Brute force	1993	Rulison and Flagan	Linear	Stainless steel	8			
Brute force	2008	Kelly et al	Circular	Fused silica	19	500 $\boldsymbol{\mu m}$	20 $\boldsymbol{\mu m}$	30 mm
Silicon micromachining	2006	Deng et al	Planar	Silicon	91	675 $\boldsymbol{\mu m}$	120 $\boldsymbol{\mu m}$	
Silicon micromachining	2017	Grustan-Gutierrez et al	Planar	Silicon	64	2 mm	40 $\boldsymbol{\mu m}$	300 $\boldsymbol{\mu m}$
Subtractive manufacturing	2013	Lojewski et al	Linear	Brass, Aluminum, PC	51	500 $\boldsymbol{\mu m}$	50 $\boldsymbol{\mu m}$	300 $\boldsymbol{\mu m}$

1.2.2 Emerging techniques for MES device fabrication

1.2.2.1 Additive Manufacturing

Recently, the rapid development of additive manufacturing enables researchers to conveniently realize their design when traditional subtractive manufacturing processes have difficulty or simply unable to handle the task. By adding the material layer by layer, the additive manufacturing method could achieve complicated structure inside an enclosed space. Velásquez-García (2015) 3-D printed a planar array of 236 internally fed electrospray nozzles within 1 cm^2 utilizing stereolithography. The configuration of each polymer electrospray

capillary along with parameters of the emitter can be easily adjusted by modifying the STL model. Olvera-Trejoab and Velásquez-García (2016) successfully fabricated the first reported MEMS multiplexed coaxial electrospray emitter consists of 25 nozzles. Coaxial electrospayring is the technique aiming at atomizing two immiscible liquids by feeding them with symmetric microfluidic channel. The liquid flow structure is as shown in Figure 5 (d). Utilizing the additive manufacturing technology, especially stereolithography to "grow" nozzles with complex inner structure is indeed remarkable, but the limitation of operational nozzle materials and the warring durability of 3-D printed nozzles are challenges remain to be addressed.

Table 2: Characteristic summary of additive manufacturing MES approaches

Year	Authors	Configuration	Nozzle material	n	P	ID	L
2015	L.F.	Planar	Polymer	236	700 $\boldsymbol{\mu m}$	377 $\boldsymbol{\mu m}$	12 mm
2016	Olvera-Trejoab	Planar	Polymer	25	3 $\boldsymbol{mm}$	450 $\boldsymbol{\mu m}$	2 mm

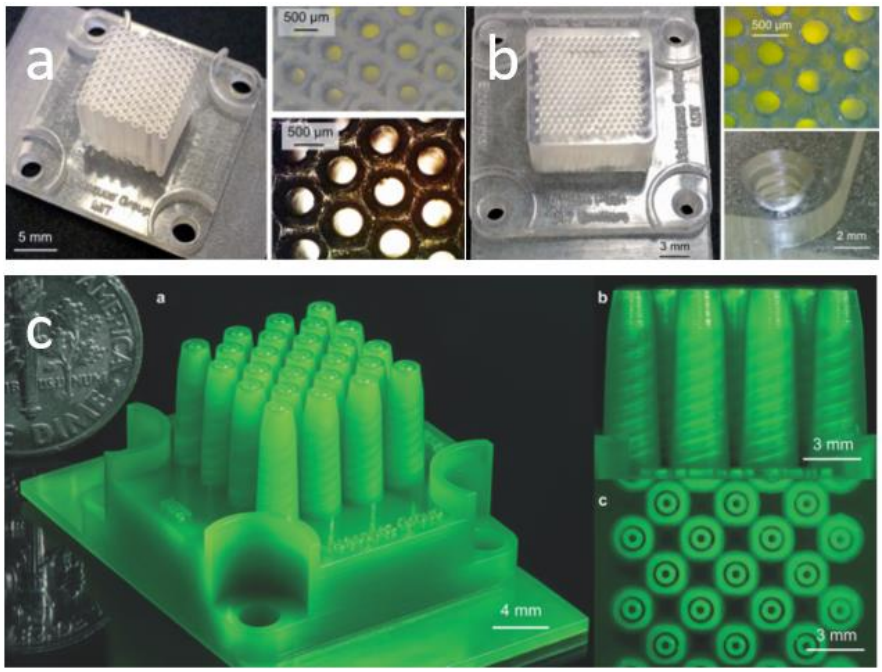

Figure 5: Image of additive manufactured MES emitters: (a),(b) polymer MES emitters; (c) coaxial MES emitter

1.2.2.2 External wetting

Liquids for emitters reviewed above were all supplied by flow resistive channels inside the supportive materials. Hill and co-workers developed dense, monolithic and planar arrays of externally-fed electrospray emitters with an integrated extractor grid and carbon nanotube flow control structures [12] . Single emitters consists of silicon solid cores and conformal CNT forests covering the surface of the core. Such structure enables liquids to be delivered through the external surface of the emitter but lacking in the controllability of the flow rate.

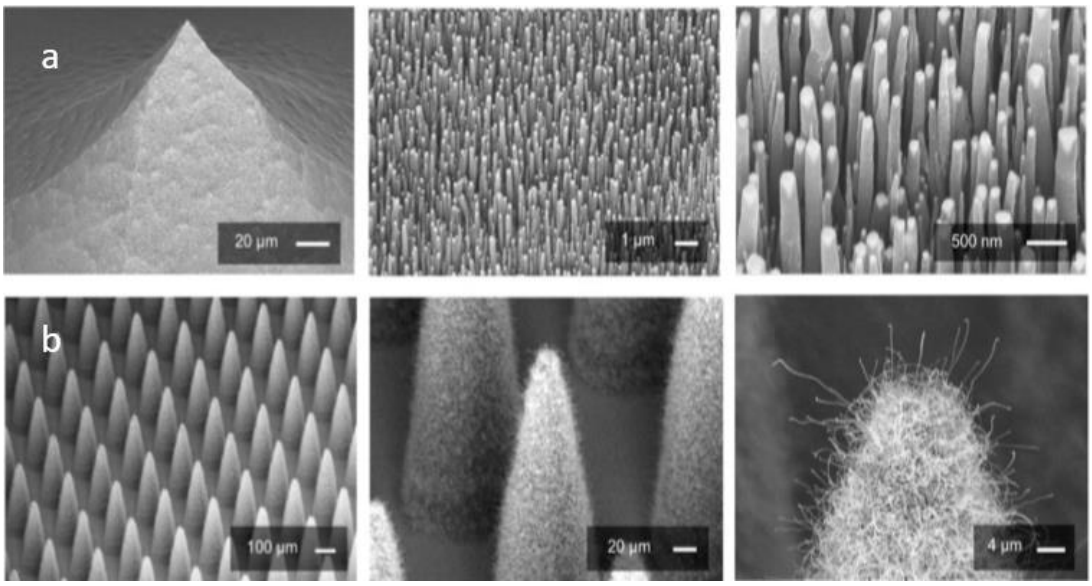

Figure 6: (a) SEM images of an emitter that is part of a sparse emitter array, along with close-up images of the CNTs grown on the emitter surface; (b) SEM images of a dense array of emitters coated with CNTs, along with close-up images of a single emitter and emitter tip. [12]

1.3 Deposition of thin film Perovskite: an example of highly corrosive and conducting liquid in need of MES

Recently, solar cells based on low-cost polycrystalline perovskite semiconductors have gone through a rapid surge in efficiency. Within seven years, the power conversion efficiency of perovskite solar cells has increased from 3.8% to 20% (Figure 7), surpassing organic PV and dye-sensitized solar cells (DSSCs) .

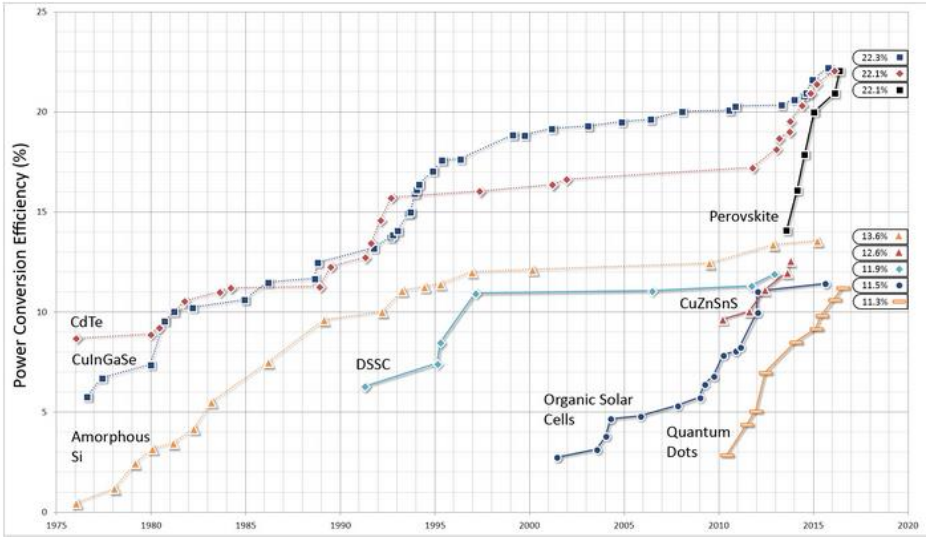

Figure 7: The graph shows a meteoric rise compared to most other technologies over a relatively short period of time. In the space of three years, perovskite solar cells have managed to achieve power conversion efficiencies comparable to Cadmium Telluride, which has been around for nearly 40 years. [13]

1.3.1 Perovskite semiconductor and its excellent properties

Perovskite [14] may refer to any material that adopts the calcium titanium oxide (CaTiO3), or ABX3 crystal structure (Figure 2 a). The particular perovskite used in photovoltaic devices is a hybrid of organic (A), metal (B) and halide (X) compounds. The most common photovoltaic perovskite compositions include methylammonium lead iodide (CH3NH3PbI3), methylammonium lead chloride (CH3NH3PbCl3), or a mixture of the two.

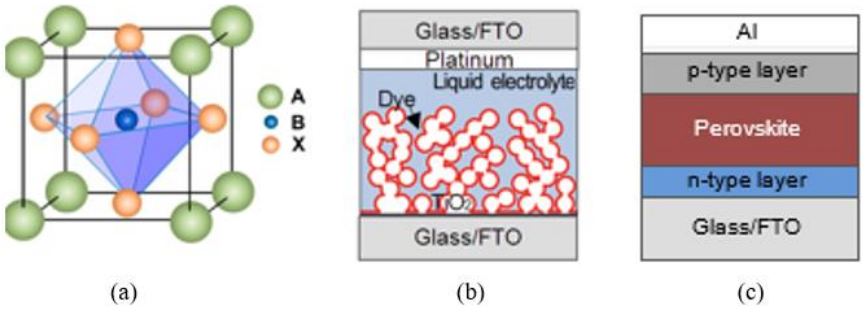

Figure 8: (a) Perovskite structure [15] (b) Classic DSSC with complex nano/meso structure of ~10 µm in thickness [16] (c) Planar perovskite device (side view) [17]

The evolution of perovskite solar cells is a remarkable example of "simple is beautiful". In 1990, Grätzel [16] pioneered dye-sensitized solar cells (DSSCs) using a sophisticated structure that consists of a ~10 μm thick porous layer of TiO2 nanoparticles sintered at ~450°C to form an interconnected 3D network, which is coated with organic dye as light absorber and soaked in an iodide electrolyte solution hole transporter. In the past 10 years, DSSC efficiencies have plateaued in the 11~12% range (Figure 7, blue squares). Recently three important findings have changed the course of DSSC research and have driven the surge of perovskite solar cells. First, in 2009, Miyasaka showed perovskite is an effective light absorber that can replace the organic dyes used in DSSCs [14], albeit with a modest 3.8% efficiency. Second, in 2012, the troublesome liquid electrolyte (a concern for leaking) was replaced with a solid hole transporting layer thereby enabling all solid-state DSSCs. Third, later in 2012, perovskite was found to exhibit charge separation and transport functionality, thereby rendering porous TiO2 scaffold layers unnecessary [18]. Together these findings led to a remarkable breakthrough: solar cells based on a 380 nm thick planar perovskite structure deposited by CVD with a record efficiency of 15.4% in 2013.

The high efficiency of perovskite solar cells is partially attributable to its unique organic-inorganic hybrid nature. While the organic component improves solubility and facilitates self-assembly from solution, the inorganic component provides strong covalent and/or ionic interactions (as opposed to weaker forces such as π–π interactions in polymer solar cells) to form a high degree of crystallinity within thin films [19]. Consequently, perovskites exhibit a set of highly desirable properties such as high open circuit voltage, strong light absorption, moderate processing temperature, high charge carrier mobilities and long charge carrier lifetimes [17]. Most importantly, the long charge diffusion length (~1 μm) closely matches the light absorption length (400 nm). This enables planar architectures [17] to achieve record efficiency without the need for complex nanostructured architectures.

Table 3: Comparison between perovskite and other solution processable photovoltaics [20-25]

Properties	Perovskite	DSSC	OPV	Implications
Open circuit voltage V_{OC} (V)	1	0.6	0.6	High V_{OC} simplifies power converter design and reduces converter costs
Optical absorption coefficient at 550 nm (cm^{-1})	$1.5x10^4$	10^3	10^5	Large optical adsorption coefficient means only very thin layers (~300 nm) are needed for complete light absorption
Charge carrier mobility ($cm^2/V{\cdot}s$)	33	1	$3x10^{-4}$	Higher mobility translates to photogenerated charge carriers more efficiently swept out of the solar cell by built-in electric fields
Diffusion length of charge carrier or exciton (nm)	100 to 1000	>1000	10	Large diffusion length enables more efficient charge collection
Optical band gap (eV)	1.55	1.8	1.9	Adequate band gap can cover majority of the solar irradiation spectrum
Processing temperature (°C)	~100	450	100	Lower temperature reduces energy consumption, enables flexible substrates for continuous R2R manufacturing and integration with other materials for tandem cell architectures

*****DSSC data is based on TiO_2 and N719 dye [16-18]; #OPV data is based on polythiophene (P3HT)[20]. Inorganic thin film materials (Si, CIS, CdTe, and CIGS) are not compared here because they are generally not processed from solutions.

1.3.2 The need an feasibility of creating perovskite thin films by electrospray

Perovskite can be solution processed at moderate temperature (~100°C) and atmospheric pressure (although some steps may require N_2 environment). These relaxed processing conditions expand the selection of compatible substrates thereby enabling technologies such as roll-to-roll (R2R) fabrication and tandem solar cells, in which perovskite layers can be printed on other established PV devices such crystalline silicon, cadmium telluride (CdTe) or copper indium gallium selenide (CIGS) to achieve device efficiencies exceeding 20% [15].

For solar energy to be competitive, the processing techniques must be continuous and scalable, such as with a roll-to-roll manufacturing platform. Presently, the dominant solution processing approach for perovskite is spin coating, which has been successful in a laboratory setting but is limited by device areas and excessive material waste. The scalability challenge arises primarily from the fact that the perovskite layer needs to be thin, ~300 nm for optimal

performance, which demands the building blocks be very small. At the laboratory scale, chemical vapor deposition (CVD) and vapor-assisted deposition can produce complete film coverage because in both cases the building blocks are atoms and molecules. However, slow growth rate (~10 nm/min) in both cases makes these difficult as viable choices for industrial scale manufacturing. A proper trade-off between the size of building blocks and throughput is critical.

Members of our lab (Yuanyuan Jiang, Cheng Li, and Weiwei Deng) have successfully formulated a perovskite precursor solution suitable for electrospray. The solution consists of Methylanmmonium Iodide ($CH3NH_3I$) and PbCl2 dissolved in dimethyl-sulfoxide (DMSO). After drying and annealing, this precursor is expected to produce a mixture of CH3NH3PbI3 and CH3NH3PbCl3, with a combined formula of CH3NH3PbI3-xClx (the value of x is small, on the order of 0.02 [26]). The doping effect of Cl- is desirable for increasing the charge carrier diffusion length from 100 nm to 1000 nm, although the underlying mechanism for this improvement remains an open question [27].

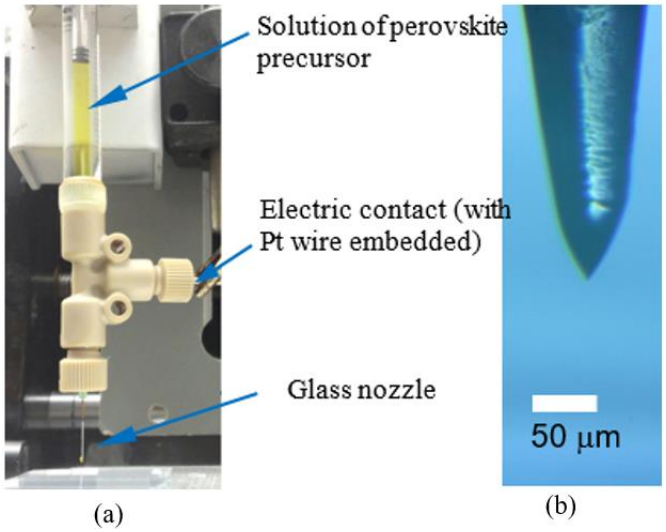

Figure 9 : (a) Experimental setup for ES processing of perovskite film. (b) The Taylor cone, which is visualized by a long working distance microscope objective lens coupled with a Canon 650D camera. The resolving power is 1 μm/pixel. The jet is too small to resolve. (Unpublished results)

The electrical conductivity of this yellow-color solution is 0.04 S/m, which is large by electrospray standards. This suggests the ES should be operated at low flow rates and with a small diameter nozzle necessary to ensure stability. We used a pulled glass nozzle with tip pulled to 50 μm. Because of the Pb2+ ions in the precursor solution, an inert conducting material (such as platinum) must be used as electrical contact. We have a platinum wire inserted in a polyether ether ketone (PEEK) tee connector (Figure 9 a) to form the electrical contact. With this setup, very stable cone-jet electrosprays can be established (Figure 9 b) at a flow rate of 5 to 200 nL/min, corresponding with an estimated droplet diameter in the range of 70 to 200 nm.

The substrate used is fluorine-doped tin oxide (FTO)-coated glass with a layer of spin-coated PEDOT: PSS as the charge transport material. Note that DMSO does not dissolve PEDOT: PSS. The substrate is mounted on a motorized linear stage and passes under the electrospray to produce a wet film. Mass conservation suggests that $\delta = Q \cdot \phi / (w \cdot v)$, where δ is the film thickness, Q is the flow rate, ϕ is the volume concentration, w is the printing width and v is the substrate speed. Hence, the film thickness can be precisely prescribed. Here, a 300 nm thick film is achieved using v=0.5 mm/sec, Q=150 nL/min and w=3 mm. The deposition rate based on this setup is ~1 μm/min per electrospray covering a 3 mm x 20 mm stripe. To put this number in perspective, the growth rate of CVD is ~10 nm/min [17].

After deposition, the wet film is heated to 100°C in an open N_2 environment. Figure 10 (a) shows the perovskite film after annealing. The sample exhibits signature brown color of perovskite. Because the drying is not regulated in the preliminary study, it is not surprising that pin-holes are observed (Figure 10 b). The film exhibits ~0.7mm edge effect, which refers to the gradual transition from the edge of the film to normal thickness. The 1.5 mm center region has uniform thickness of ~320nm measured by a profilometer. Most importantly, X-ray diffraction (XRD) peaks of the printed sample at 14.1°, 28.4° and 43.2° are in excellent agreement with⟨110⟩, ⟨220⟩ and ⟨330⟩ peaks of the mixed-halide perovskite with an orthorhombic crystal structure. A high level of phase purity is indicated by the fact that no measurable ⟨001⟩ diffraction peak for PbI (12.65°) and ⟨110⟩ diffraction peak for CH3NH3PbCl3 (15.68°) are detected. This is strong evidence that electrospray deposition and subsequent drying (despite being unregulated) can indeed deposit polycrystalline perovskite.

Our lab's preliminary results show that ES can process perovskite precursor into thin films several hundred nanometers thick at a high growth rate. These results demonstrate the feasibility of using ES to process perovskite precursor and set the stage for studying MES emitters for highly corrosive and conducting liquids.

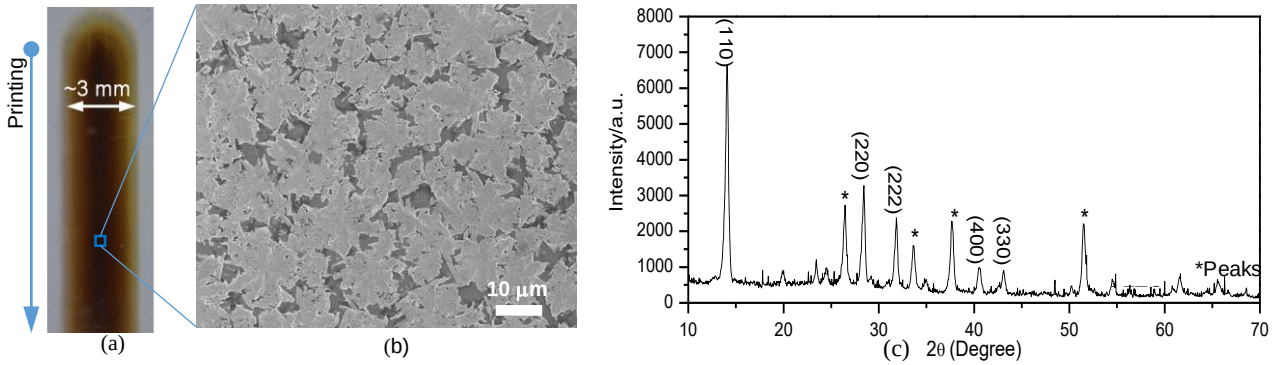

Figure 10 : Solid film of electrospray deposited perovskite (a) Optical image, the half circle at the top is where the ES started; (b) Scanning electronic microgram (SEM), with dark color as ruptured area; and (c) X-ray diffraction (XRD). Unpublished results.

1.4 Thesis overview

After considering these techniques for MES emitters machining, we chose to use laser as our primary tool to fabricate nozzle arrays. We also use 1.5 mm thick conductive silicone sheet as the raw material because of its inert characteristic. The unique advantage of laser microfabrication technique is that it balances the precision, scalability, efficiency and cost well. Compared to the brute force method, laser microfabrication is able to achieve very flexible design process and better scalability. For example, it takes a fiber laser marker less than 30 minutes to machine a planar array of 256 nozzles, which is superior than silicon microfabrication regarding both time and costs.

Chapter 2 focused on the fundamental study of crucial characteristics of the fiber laser marker for micromaching of conductive silicone sheets. The general purpose laser system was modified to meet the requirement of the precise and clean machine process. Then detailed laser

milling techniques needed for machining external structure on the 1.5 mm thick silicone sheet was presented.

Chapter 3 discussed the machine technique related to the fabrication of the microfluidic channels with high pressure drop including through holes on silicone sheets and in-plane microfluidic channels on silicon wafers. To evenly distribute the liquid into multiple cone jets, the flow resistance within the channel must be comparable to the surface tension at the nozzle tip. Thus by evaluating the flow resistance and surface tension, we were able to determine the dimension of our microfluidic channels under a certain flow rate and fabricated them with appropriate laser parameters.

In Chapter 4, the design and implementation of silicone based MES emitters was introduced. We utilized the three-electrode design (distributor-extractor-collector) and integrated the emitter with a simple but efficient process. By carefully designing each component, we successfully implemented a linear array up to 16 emitters.

Chapter 5 demonstrated cone-jets and spray profiles of different nozzle array configurations. Among all nozzle configurations tested previously, nozzles with 300 μm outer diameter performed the best on generating stable cone-jets. Thus, we further measured the uniformity of the cone-jet diameter. The result showed that there was an approximate 20% variation between the flow rate of each nozzle for nozzles with 55 μm OD and 300 μm ID.

In Chapter 6, we summarized findings made in this work

CHAPTER 2: Laser micromachining of nozzle external structure

Ever since the first laser was introduced by Maiman at 1960s [28], this technology has been growing rapidly both for research and industrial purposes. Fiber lasers are relatively new addition to traditional CO_2 or solid-state laser [29]. Here, we modified a 10W RGL-FM Series Fiber Laser Marker as a versatile machine tool. This tool is able to handle machine tasks such as drilling, milling, engraving and even welding. The galvanometer system enhanced the precision of the laser, which enabled us to freely change laser path parameters. This chapter aims at finding the appropriate parameters for fast and clean material removing tasks because silicone was prone to damage by high energy density.

Sections 2.2 and 2.3 covered the entire silicone nozzle laser milling process flow including the plane milling, the nozzle outline milling and the post-cleaning process. Meanwhile, imperative machine process and parameters were also presented to assist the comprehension. The study eventually enabled us to mill the 18×18 dummy nozzle array as shown in Figure 19 in less than 30 minutes.

2.1 Machine tool

The 10W RGL-FM Series Fiber Laser Marker is a flexible direct marking machine. The ability to change various laser parameters offers numerous choices in control, quality and speed. However, the original configuration of this general purpose fiber laser maker was unable to handle precision micromachining tasks. We made the following modification to substratinally increase the machining precision and accuracy. First, we reduced the focal length of the original field lens to achieve a tighter focus and a higher energy density. Second, a 3-axis microstage was mounted on top of the original cross-scissor jack that enabled us to precisely control the location of the workpiece. This modification led to several changes in controllable parameters, which was listed in Table 4.

2.1.1 Principles

The RGL-FM fiber laser marker system is equipped with independent X-Y axis galvanometers to implement multi-layer milling and rotary drilling as shown in Diagram 1. The 1064 nm infrared laser beam is able to machine a variety of materials, including many kinds of metals, plastics, ceramics, natural stones, and leathers. The laser beam generated by a fiber laser has already been coupled with a flexible fiber, which is very convenient in terms of laser beam delivery. The beam expander first expands the beam emitted from the fiber. Two sets of galvanometers positioned in an orthogonal direction control the position of the beam in X and Y direction separately. After passing through the field lens, the laser beam following the Gaussian distribution will have the minimum beam diameter right at the focus of the lens. Then the focused laser beam with only 12 μm in diameter can precisely remove the material by melting and vaporizing.

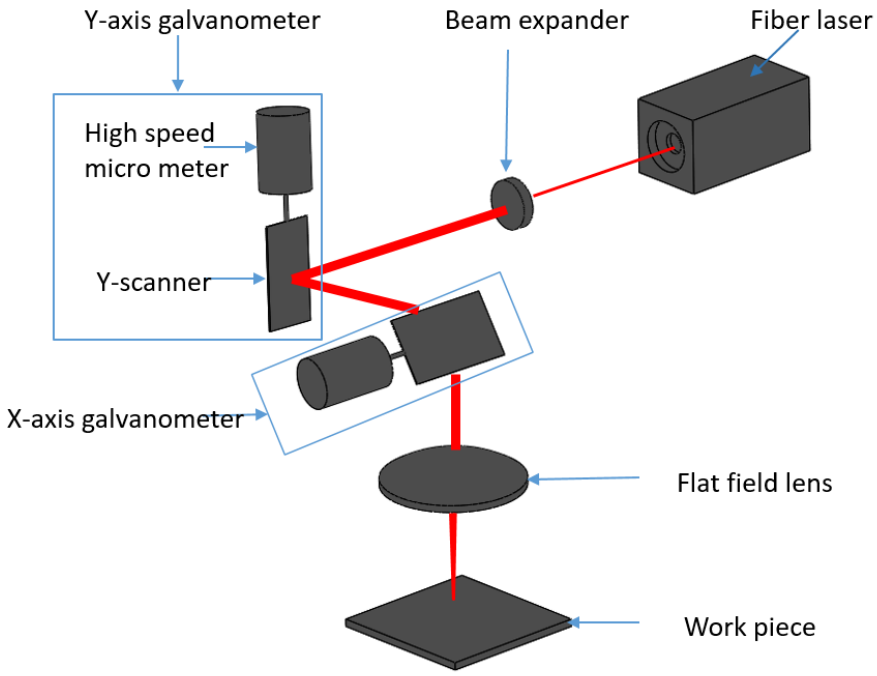

Diagram 1: Fiber laser marker operation principle

2.1.2 System Modification

Figure 11 Modified 10W RGL-FM Fiber Laser Marker

2.1.2.1 XYZ Stage

To precisely control the distance between the field lens and the workpiece surface, a precision 3-axis micrometer-positioning stage was mounted on the original cross-scissor jack. The introduction of the stage with 20 μm minimum step made it possible to study the performance of this system when the workpiece is located at the different relative position.

2.1.2.2 Field Lens with 100mm EFL

The original filed lens with 163mm Effective Focus Length (EFL) was replaced by another one with 100mm EFL. Focused beam diameter decreased from 20 microns to 12 microns due to the change of EFL, which increased the power density by 2.6 times from 125J/cm^2 to 325J/cm^2.

2.1.3 Process Parameters

The change of the EFL not only decreased the minimum beam diameter and increased the power density, but also decreased the maximum scan speed. Modified process parameters of the re-configured fiber laser marker were listed in Table 4.

Table 4: Parameters of modified the RGL-FM fiber laser marker

Parameters	Range
Scan speed	0-6000 mm/s
Average power	10 W
Peak power	2.5 KW-10 KW
Frequency	20 KHz-80 KHz
Focus diameter	12 **µm**
Energy per pulse	0.5mJ
Energy density	325J/$\boldsymbol{cm^2}$

Changeable parameters in Table 1 included scan speed *(V)*, peak power *(PP)*, frequency *(f)* and spot gap *(δ)*, where δ is the distance between the center of two consecutive laser spot defined by the following equation [30]:

$$\delta = \frac{V}{f}$$

2.2 External structure milling

Using laser beam as the machine tool, laser milling provides fine accuracy without involving any mechanical contact, effluents or machine tool wearing problem. After being converted to STL files, CAD models can also be used to assist the machining of complex structures as shown in Figure 12. In the present laser milling studies, tests were carried out on conductive silicone sheet for nozzle milling purpose. Unlike the through hole drilling process presented in the next chapter, milling nozzles from silicone sheet required material removal using high scan speed and low power level to ensure smooth machined surface. Then specific influence factors including scan strategies and power level were studied to improve the edge finish quality of nozzles. After the milling process, nozzles needed to be thoroughly and gently cleaned before being integrated into the electrospray system. The silicone debris exhibit strong adhesion to the nozzle, and the simple ultrasonic cleaning process was unable to thoroughly clean the surface of the nozzle especially the top surface of the nozzle. Thus a drop-wipe process was added after the ultrasonic cleaning process (Section 2.2.4).

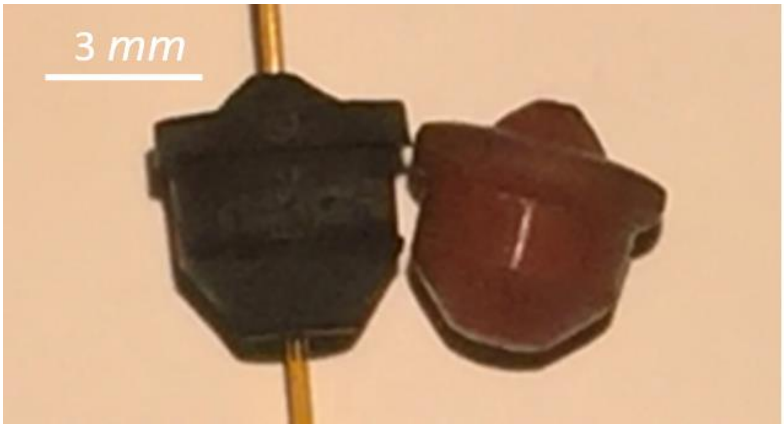

Figure 12：Laser milled conductive sealing part (left) and the original rubber part (right)

2.2.1 Surface topography

The surface topography of the laser milled area was determined by a complex interaction of multiple factors. Initially, the experiment was focused on how the pulse overlap and the step overlap influenced the surface topography. We intend to identify critical process parameters for the milling that generates surface finish as smooth as possible. The “Step” represents the distance between two neighboring parallel laser paths (shown in Figure 13) while the “Step overlap” refers to the overlapping region between laser spots from two neighboring laser paths. The test result showed that low scan speed with low Step offered smoother surface finish. However, applying both the scan speed and the step at a relatively low level would apparently increase the total milling time especially for large area milling. A relatively high scan speed of 420mm/s under 20 KHz and low step at 7 μm were adopted for balancing the machining efficiency and surface quality while the surface roughness could still be controlled under 2μm (Figure 14).

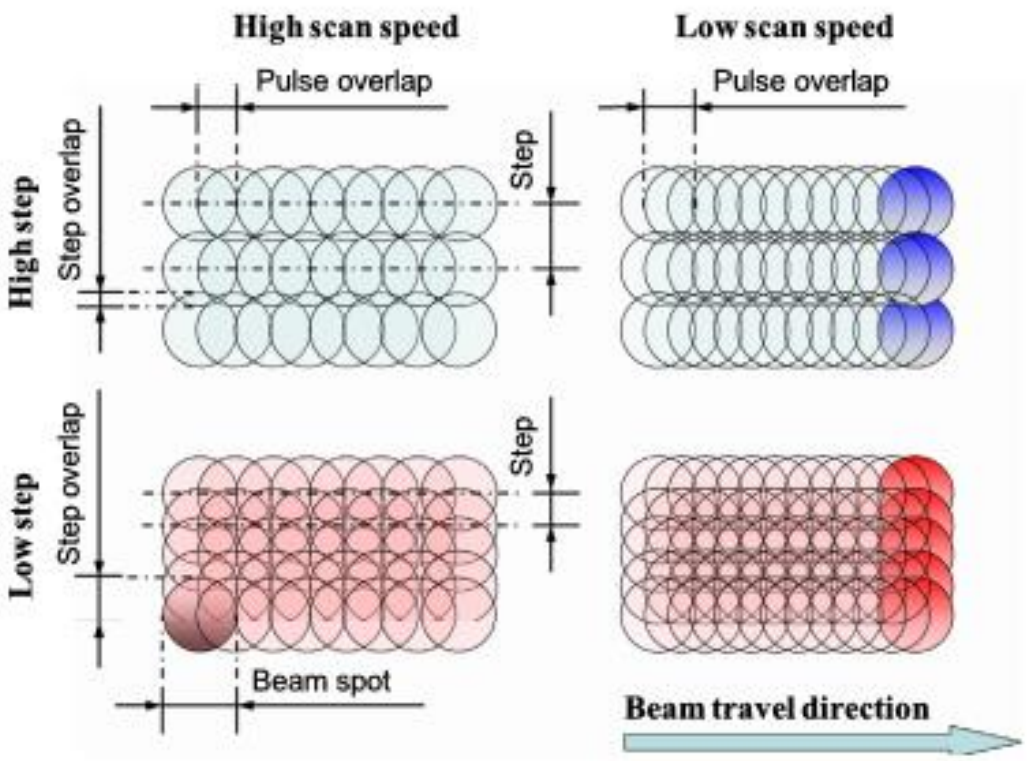

Figure 13 : Illustration of the step, pulse overlap and step overlap [31]

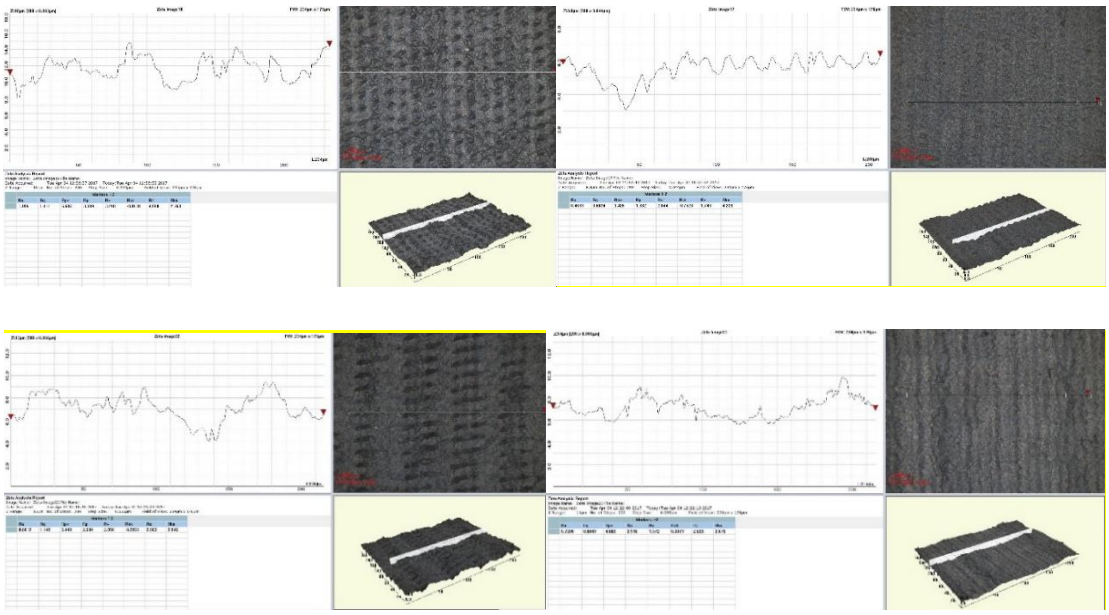

Figure 14: Surface topography of milled surface machined under (a) high step with high scan speed; (b) high step with low scan speed; (c) low step with high speed; (d) low step with low speed

2.2.2 Laser beam scanning strategy

Single nozzle quality is critical for the stability of cone jets during the electrospray process. The quality of laser milled nozzles needs to be comparable with the nozzle array made by traditional machining methods. Thus, different laser beam scanning strategies and corresponding milling parameters were studied.

The linear laser scan pulses are simple to design but improper for milling nozzles. Hackly edge caused by the end pulse of each machine line deteriorated the quality of the entire nozzle. Thus, two alternative circular laser beam scan strategies were introduced: circular scan path (Figure 15(a)) and spiral scan path (Figure 15 (b)). Circular scan path was first used for the milling of nozzles with 150 μm in outer diameter (OD) whose top finish of the nozzle is shown in Figure 16 (a). 150 μm was also the minimum outer diameter of the laser machined silicone nozzle with acceptable surface quality. Even though the surface quality of the nozzle had been significantly improved, an apparent default of this strategy revealed by Figure 16 (b) indicated that a thin redundant membrane existed at the start point of each independent circular laser path. Such default was caused by the activation delay of the laser beam and galvanometer scanner. Thus, an additional precision milling process was needed for the removal of this redundant membrane when applying circular path. The spiral path was identified to be an improved strategy. Such machining process consisted of one single laser path without involving laser initiation and step motion of galvanometer. However, the nozzle machined with this scanning strategy had an ellipse shape rather than a circular outline as shown in Figure 16 (c). By decreasing the spiral path density at the inner ring through the graphical user interface (GUI), this default can be barely observed for nozzles with 300 μm OD or larger Figure 17 (c).

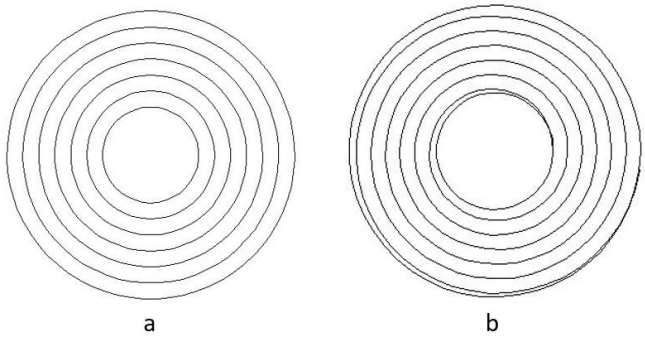

Figure 15: (a) Circular scan path, (b) spiral scan path

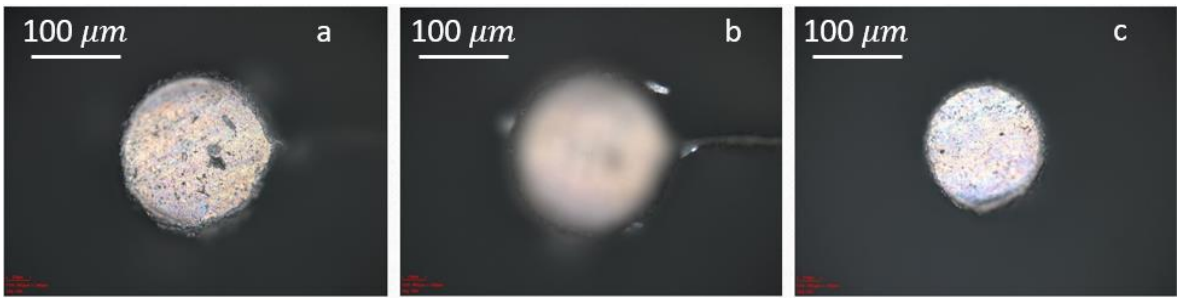

Figure 16: Top view of nozzles machined with: (a) (b) circular path; (c) spiral path

2.2.3 Power level

The power level was another crucial parameter that influenced the edge quality of a nozzle. Figure 17 shows the top view of a few dummy nozzles milled under decreasing power level. Generally, the lower the power level was, the cleaner the nozzle edge would be. However, decreasing the power level also decreases the material removal ability of the laser, which means more path numbers needs to be applied. Balanced parameters for milling nozzles with the outer diameter of 300 μm and the height of 600 μm is shown in Table 5.

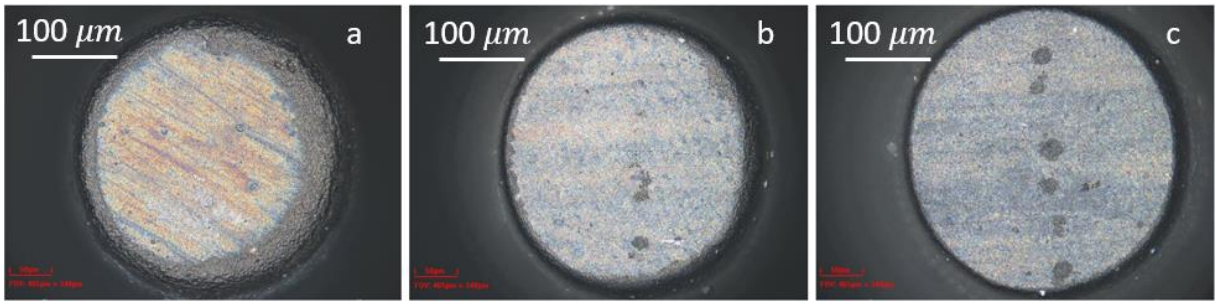

Figure 17: Dummy nozzles machined under (a) 100% power; (b) 50% power; (c) 2% power

Table 5: Milling parameters for nozzles with 300 μm OD

Parameters	Power level	Scan speed	Pulse frequency	Milling depth per path	Path number
Values	2%	110 mm/s	20KHz	50 μm	12

2.2.4 Post cleaning process

After nozzle machining, post cleaning was required prior to device assembly. The entire nozzle array would be submerged in a bath of ethanol and ultrasonically cleaned for half an hour right after the milling process. After being dried with compressed air, the surface of the nozzle shown in Figure 18 (b) was still covered with a thick layer of silicone debris. Such nozzles would cause liquid flooding or electric sparks during electrospray tests. Thus, the process of top-surface drop-wipe using lens wiper was adopted after the ultrasonic cleaning. However, such contact cleaning method could not be applied on nozzles with 150 µm OD due to possible irreversible damage.

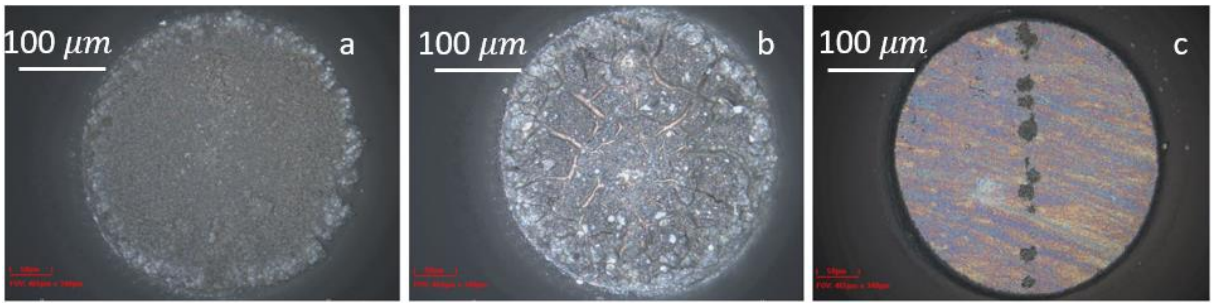

Figure 18: 300 µm nozzle top finish (a) right after the milling; (b) after ultrasonic cleaning; (c) after lens wiper cleaning

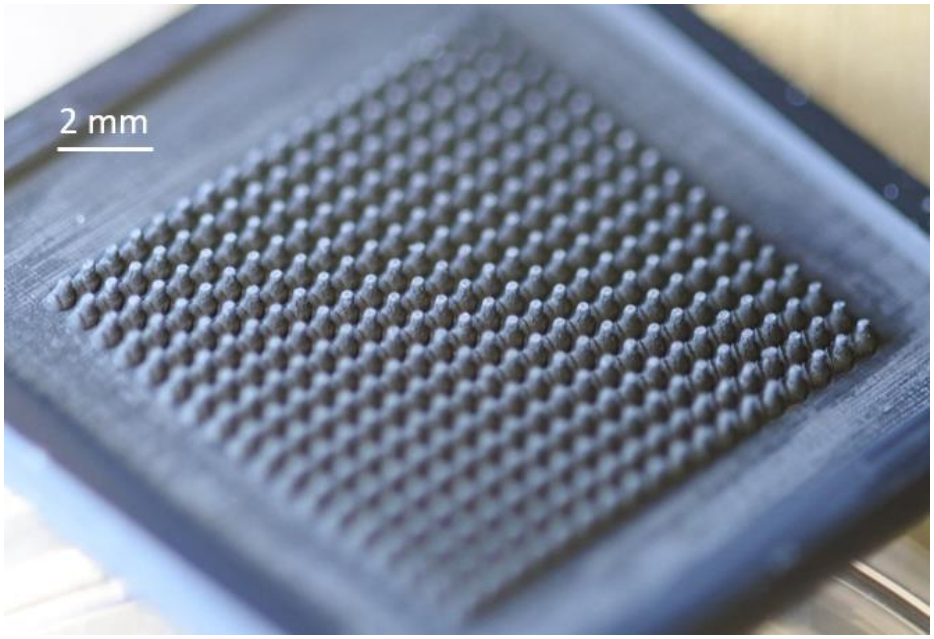

Figure 19: 18×18 dummy nozzle array

Chapter 3 Laser Machining of Channels with High Flow Impedance

To evenly distribute the liquid from the common reservoir into all nozzles, a design rule established by Deng, Waits and Gomez (2009) should be satisfied: the viscous pressure drop through the channel, given by the Hagen- Poiseuille Equation, should be comparable to the electrohydrodynamic pulling pressure, which is comparable to the surface tension pressure at the nozzle tip. This gave us the crucial design rule for the parameters of the flow-resistive channel. There were mainly two methods to increase the flow resistance: decreasing the inner diameter of the nozzle or adding an individual microfluidic channel for each nozzle. The dimension of the channel cross section dominated the pressure drop within both flow-resistive channels. For through holes, the pressure drop was very sensitive to the inner diameter ($\Delta P \sim ID^{-4}$). For microfluidic channels, the pressure drop was dominated by the depth of the channel ($\Delta P \sim H^{-3}$) but also inversely proportional to the width of the channel. The laser drilling process on the silicone sheet was studied systematically. The variation of the diameter for through holes with 50 μm OD was decreased to 5%. For the individual microfluidic channel for each nozzle, attempts had been made on multiple materials: conductive silicone sheets, self-fusing silicone tapes, and silicon wafer. Eventually the silicon wafer was chosen because it has the cleanest surface finish. Section 3.2 presented the detailed engraving technique for the microfluidic channel fabrication.

3.1 Through hole drilling

Most published results on laser drilling process were focused on metals or ceramics. Dubey and Yadava [32] studied the relationship between laser parameters and through hole quality on Ti–6Al–4V. Chuan-Jie Wang [33] studied how power level influenced the quality of drilled holes on Amorphous Alloys Foils. Since the flow resistance inside a nozzle is highly related to the nozzle ID ($\Delta P \sim ID^{-4}$), a slight decrease of the nozzle ID will lead to a dramatic

resistance increase along the through hole. Thus, the challenge here was to decrease the nozzle ID to the best of our ability without influencing the uniformity of the through-hole array. Unlike metal drilling process, drilling through holes on the 1.5 mm-thick conductive silicone sheet does not require special gas environment for good laser performance. For a single through hole, essential parameters including minimum diameter, finish circularity and internal surface quality were presented in each subsection. The last subsection focused on the method to study the inner diameter uniformity of a nozzle array.

3.1.1 Through hole flow resistance

The surface tension pressure at the nozzle tip is given by

$$P = \frac{2\gamma}{OD}$$

The pressure is proportional to the surface tension of the liquid and inversely proportional to the outer diameter of the nozzle. For ethanol, surface tension γ = 0.023 N/m. OD is the outer diameter of the nozzle. The minimum outer diameter of the silicone nozzle that has been successfully tested was 150 μm. However, to better distribute the flow rate as well as increasing the durability of the nozzle array, the outer diameter of the nozzle was increased to 300μm, which halve the desired pressure drop.

The viscous pressure drop through the channel is given by

$$\Delta \mathrm{P} = \frac{128 Q \mu L}{\pi I D^4}$$

The pressure drop within a through hole channel is proportional to length of the channel and inverse fourth power of the channel diameter. For ethanol the viscosity $\mu = 1.214\ mpas$. The maximum length of the channel $L = 1.5\ mm$, which is the thickness of the silicone sheet. We used ethanol to test the performance of the emitter for its low cost and good spraying ability. Eventually, the emitter will be used for spraying liquid with relatively high conductivity. Our current study indicates that for perovskite solution, the proper flow rate was 240 nl/min per nozzle. Thus, we took $Q = 4nl/s/nozzle$. For nozzles with $ID = 55$ μm and $\mathrm{OD} = 300$ μm, $\Delta \mathrm{P} = 32.4$ pa $< \mathrm{P} = 153.3$ pa . For nozzles with $ID = 30$ μm and $\mathrm{OD} = 300$ μm , $\Delta \mathrm{P} =$

$366.5\ \text{pa} > P = 153.3\ \text{pa}$. When the inner diameter of the nozzle was kept at $55\mu\text{m}$, the pressure drop was barely comparable to the surface tension at the nozzle tip. For the nozzle with 30μm ID, the pressure drop would overwhelm the surface tension and even the flow distribution.

3.1.2 Drilling parameters

With fixed pulse duration and wavelength, workpiece location, power level, and laser path diameter are three parameters that can be utilized to adjust the diameter of the through hole. For a Gaussian laser beam, the minimum beam diameter will appear at the focus of the field lens. Thus locating the exit of the through hole at the laser focus will provide the minimum exit diameter.

Figure 20 shows the typical surface topography after applying continuous single pulses onto a silicone sheet, in which the recast layer was large and thick. Instead of being vaporized by single pulses as metal or ceramics, silicone removed by the previous pulse will become debris and influence the heat absorption of the next laser pulse. Thus circular laser path was used for drilling through holes on silicone sheets. Minimum laser path diameter can be set to 7 μm to get a through hole with exit diameter as small as 20 μm (Figure 20 c). Both entry circle diameter and exit circle diameter were dependent on laser power levels. Comparing Figure 21 (b) and (c), the exit diameter of the through hole could be decreased by more than 30% for only 4% reduction in power level. However, as the diameter of the through hole being decreased, the defective rate of a through-hole array would increase. Thus for the application of multiplexed electrospray system, nozzles with 30 μm inner diameter were sufficient based on the calculation shown in the previous section.

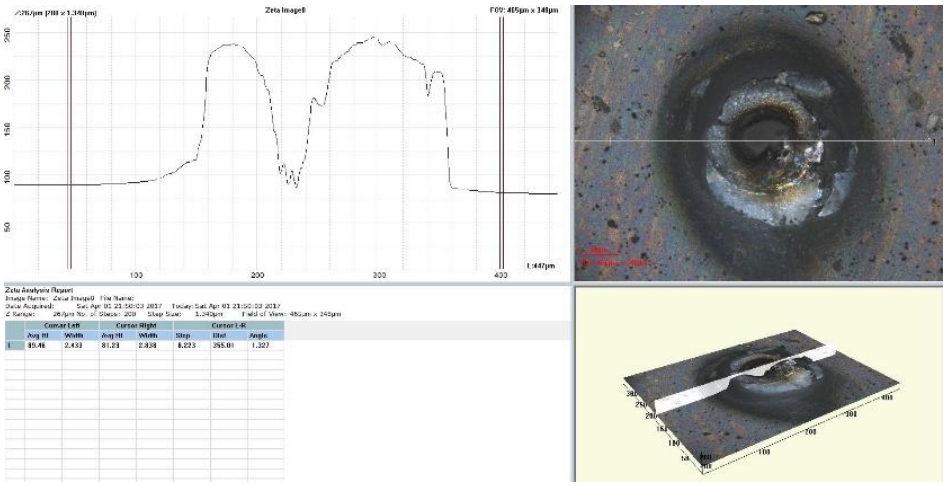

Figure 20: Surface topography of laser affected area

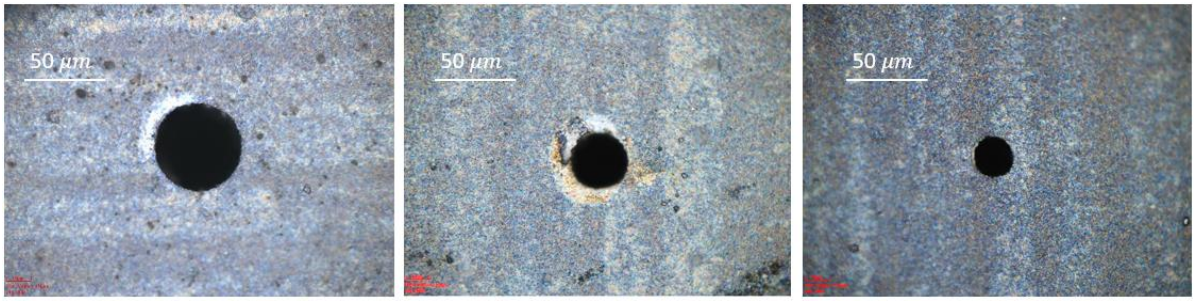

Figure 21: Through hole exit with (a) 55 µm diameter; (b) 30 µm diameter; (c) 20 µm diameter

Table 6: System parameters for through hole drilling

Parameters	55 µm	30 µm	20 µm
Power level	100%	100%	96%
Laser path diameter	10 µm	7 µm	7 µm
Scan speed	1 mm/s	0.6 mm/s	0.6 mm/s
Pulse Frequency	20 KHz	20 KHz	20 KHz
Surface-focus distance	+2.5 mm	+0.25 mm	+0.25 mm

3.1.3 Finish circularity

The typical through hole entry and exit on the silicone sheet are shown in Figure 22 (a) and (c). The circularity and uniformity were very poor at this stage compared to traditional through hole drilling process using drill bits. To solve this problem, a 120 μm thick silicone sacrifice layer was added above the entry of the through hole and a 500 μm thick silicone sacrifice layer was added below the exit of the through hole. Figure (b) and (d) shows the entry and the exit of a through hole machined under same parameters as Figure (a) and (c). By adding sacrifice layers, both the circularity and the uniformity of the though-hole array were significantly improved.

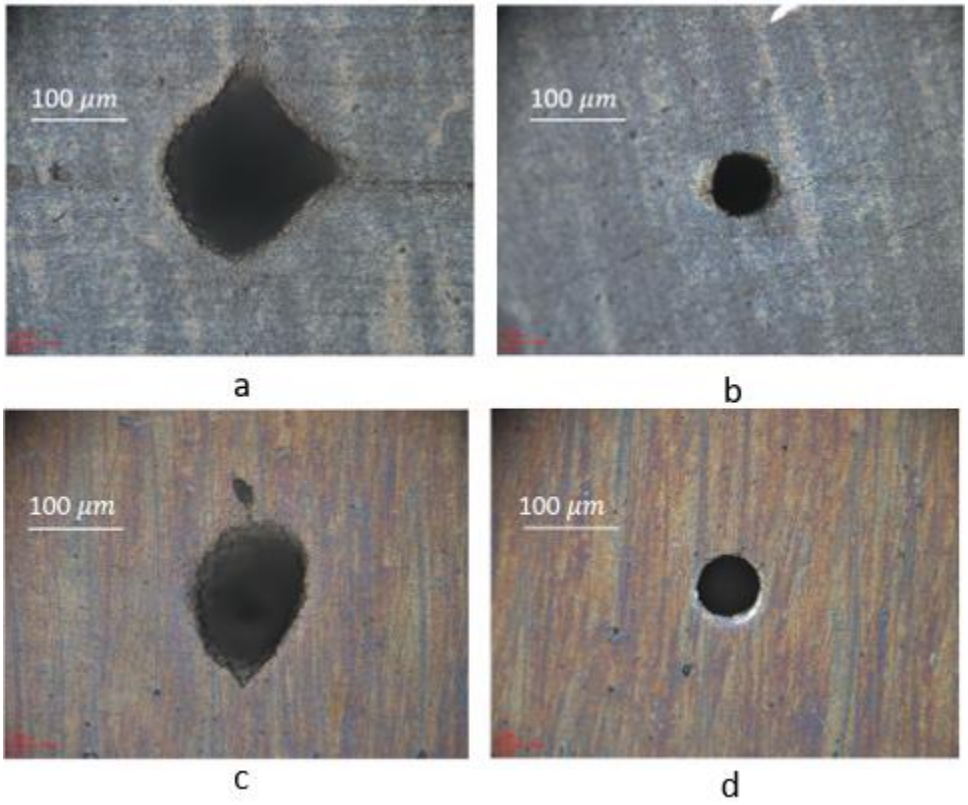

Figure 22: Through hole entry without (a), with (b) sacrifice layer; through hole exit without (c), with (d) sacrifice layer

3.1.4 Inner wall quality

Figure 23 shows the inner wall topography of a through hole with 55 μm in diameter machined under 100% power level. The inner wall quality was evaluated by the root mean

square roughness (Rq) of the inner wall along the axial direction as shown in Figure 23 (b). For through holes machined by circular laser path, the root mean square roughness of the inner wall was less than 500 nm, which is sufficient for smooth liquid flow inside through holes with the diameter of 55μm.

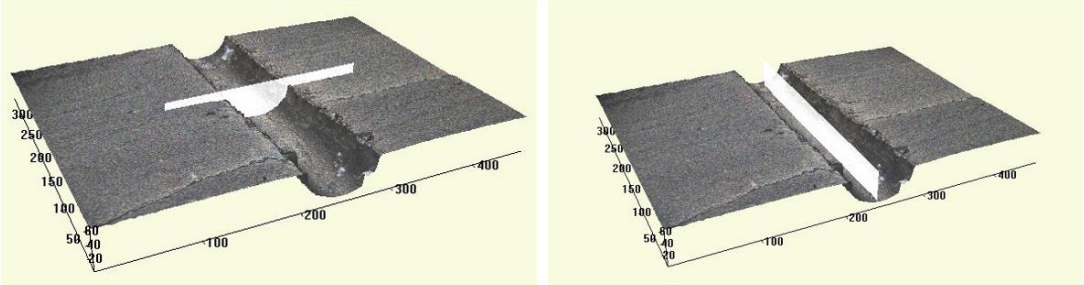

Figure 23: Inner wall topography of the laser drilled through hole

3.1.5 Through-hole array uniformity

To evenly distribute the liquid into each nozzle, the uniformity of the through holes' diameter needs to be closely examined. Since conductive silicone could be easily damaged by traditional machine methods or the laser beam, special set up as shown in Figure 24 was used to evenly cut the 1.5mm thick silicone sheet into five thin slices, which gave us six sets of diameters for one through-hole array at different depths including entry and exit. The uniformity of a through-hole array consists of 10 through holes is shown in Table 4. Even though the average diameter varies along the axial direction, the exit diameter always remained the smallest. This enabled us to monitor the uniformity of the through-hole array by simply measuring the exit diameter. Meanwhile, the standard deviation of the diameter remained the same at the different depth of through holes.

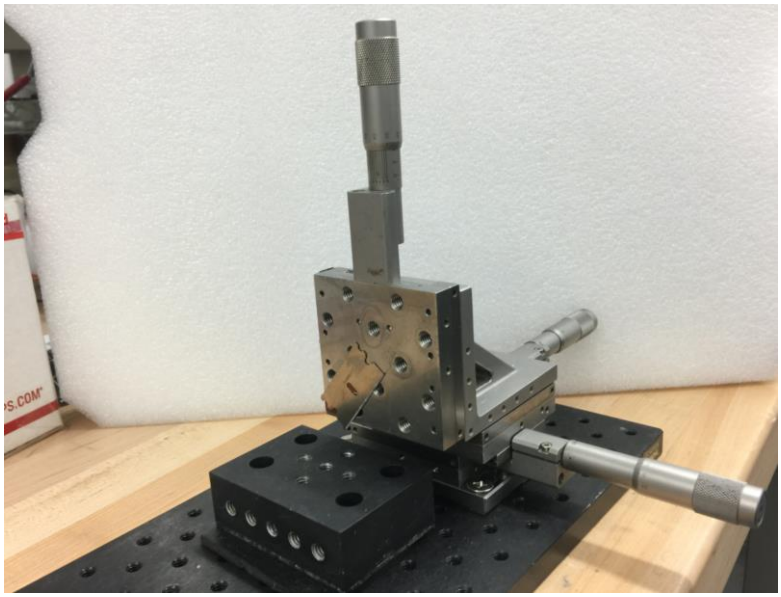

Figure 24: Nozzle array cutter

Table 7: Average inner diameter of nozzles at different depth of the material

Depth	Entry	300 **µm**	600 **µm**	900 **µm**	1200 **µm**	Exit
Average diameter/ **µm**	56.6	62.1	60.6	64.0	60.1	52.6
STDEV/ **µm**	2.3	2.3	2.3	2.3	2.4	2.4

3.2 Microfluidic channel

Uniformed microfluidic channels with proper dimensions are also able to provide sufficient pressure drop if the desired nozzle ID could not be met. The machining of microfluidic channels on silicon wafers followed the same process as silicon nozzle microfabrication [10]. To reduce the cost and complexity of the process, we utilized the same fiber laser marker to engrave the similar channel on the silicon wafer. The flow resistance was first calculated to help choose the dimension of the individual channel for each nozzle. Then

we studied fundamental properties of the silicon wafer machiend by single laser pulses. Section 3.2.3 presented the microfluidic channel we designed and fabricated with a branch pattern.

3.2.1 Microfluidic channel flow resistance

The viscous pressure drop through the channel is given by

$$\Delta P = \frac{8Q\mu L}{WH^3}$$

The pressure drop is proportional to the channel length, inversely proportional to the width of the channel and dominated by the height of the channel ($\Delta P \sim H^{-3}$). Here, we chose the channel length $L = 3.6\ mm$, the channel width $W = 80\ \mu m$ and $H = 20\ \mu m$. Noticing that it is extremely convenient to control these three parameters of the microfluidic channel, we could increase or decrease the flow resistance by changing any of these parameters. For ethanol, the viscosity $\mu = 1.214\ mpa{\cdot}s$ and the flow rate $Q = 4\ nl/s/nozzle$ for the purpose of spraying highly conductive fluids. With parameters provided, the viscous pressure drop was then estimated as $\Delta P = 437.0$ pa , which is almost three times as the surface tension (153.3 pa).

3.2.2 Systematic test of single laser spot

By applying the scan speed of 4000mm/s and frequency of 20kHz, a set of experiments were designed to study how the power level and focal point position influenced laser engraving on silicon wafers. Samples shown in Figure 25 contained 2000 lines of micro spots made by individual laser pulses. Each column of lines was machined under ten different power levels from 0.1% to 100%. Each row of lines contained 200 lines machined under different relative distance between the lens and the workpiece surface at 20 μm interval within the effective focus length.

Figure 25: Samples for studying the contribution of power level and workpiece location

3.2.2.1 Power Level

Figure 26 acquired by the profilometer shows the surface topography of the spots on the silicon wafer with gradually increased power level at the focus. When the power level was less than 10%, a black spot can be observed at the center of each spot, which was proved as volcano structures at the center (Figure 27). When the power level is higher than 40%, the severe splashes around the edge of spot and the large area of recast layers indicated that the laser beam was overpowered. Thus, the power level was controlled between 20% to 40% for the fabrication of microfluidic channels.

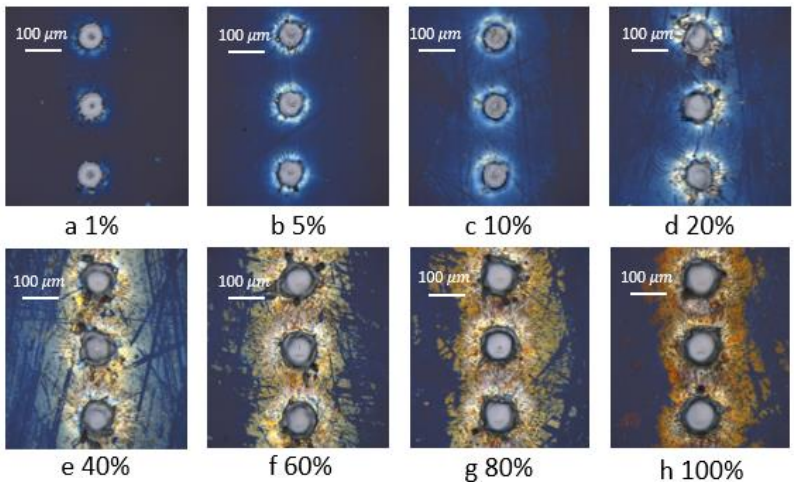

Figure 26: Material removal of single laser pulse at the focus

Figure 27 is the profile of spots machined with a few typical power levels. With the power level less than 10% of the peak power, energy absorbed by silicon wafer could melt the material but was not sufficient to vaporize the material. Thus, melted silicon would accumulate inside the spot and form a volcano shape at the center. The profile also allows us to estimate the volume of the silicon removed by a single laser pulse. The results (Table 2) indicated that the volume of silicon removed was linearly related to the power level.

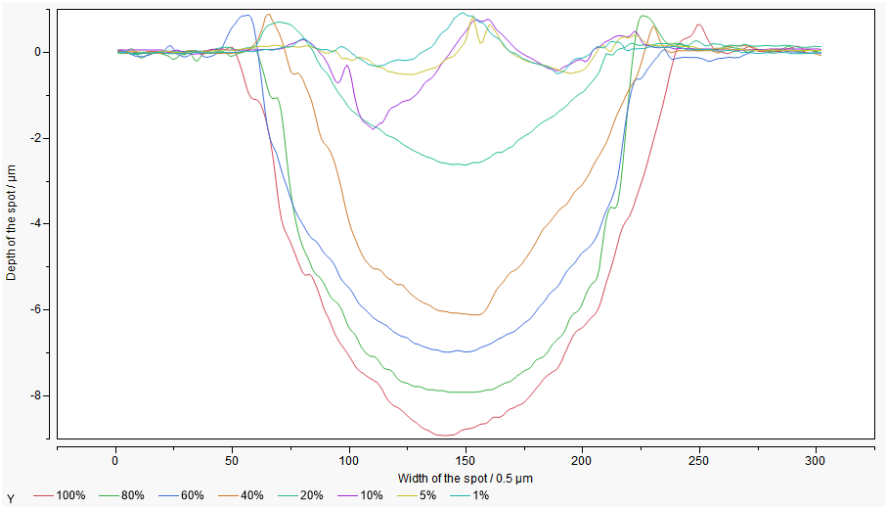

Figure 27: Cross-section of single pits under machined with different power level

Table 8: Volume of silicon removed by a single laser pulse

Power level	20%	40%	60%	80%	100%
Silicon removed/ μm^3	613	1796	2926	3410	4411

3.2.2.2 Focal point position

The distance between the surface of the workpiece and field lens had a great impact on the circularity of the spot (Figure 28). Such phenomenon would influence our estimation on the pulse overlap and step overlap (Figure 13), thereby further decreasing our controllability on the surface quality of the machined surface. Thus, the top surface of the silicon wafer was always positioned right at the focus of the field lens.

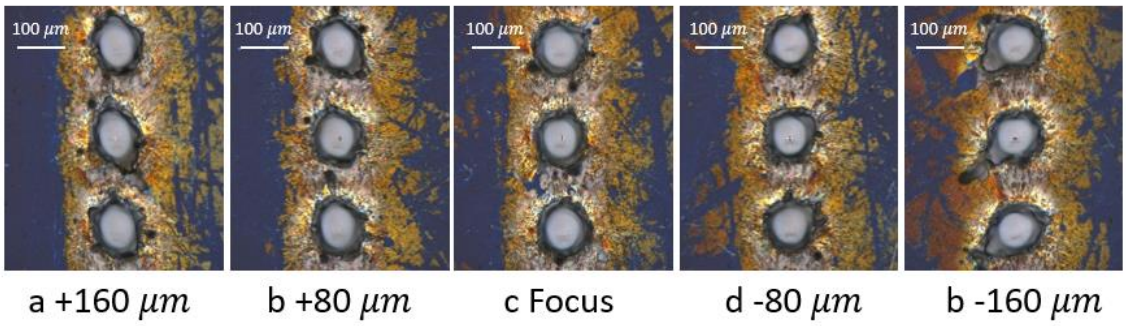

Figure 28: Surface topography of single laser spots

3.2.3 Configuration of flow-resistive channels

Here we attempted to use the laser to engrave microfluidic channel on silicon wafers. Ideally, the nozzle array can be milled on the other side of the silicon wafer and through holes will be able to connect the end of the flow-resistive channel to the surface of the nozzle. However, the attempt to shrink the diameter of laser drilled through holes from millimeter scale to micrometer scale on the 0.75 mm thick silicon wafer failed with our current inferred laser. Thus, we only used the silicon wafer with flow-resistive channels as both the reservoir and the support of the silicone distributor at this stage. The branch pattern of microfluidic channels is shown in Figure 29. The height of the channel was 20 μm. The width of the channel at the end of the branch was 80 μm while the width was doubled for each converge of the branch, which resulted in a common channel with the width of 1.28 mm.

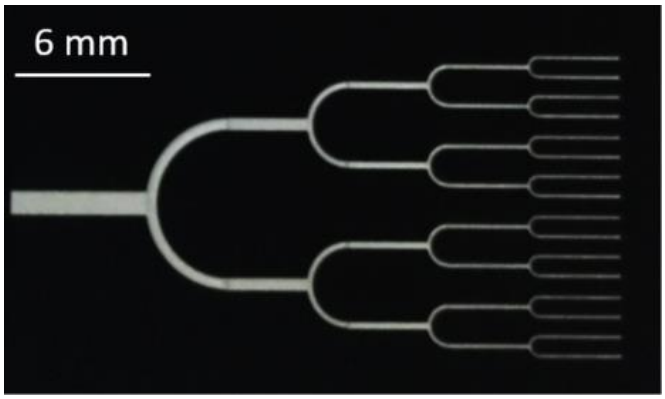

Figure 29: Microfluidic channels on silicon wafer.

Chapter 4 System design and implementation

This chapter provides an overview of the design and the fabrication process for the silicone based MES emitter utilizing three electrodes design (Figure 30). Compared to emitters made by other methods, laser micromachining provided saving in both time and costs. The total time required for fabricating a well-functioned emitter array from raw materials of each electrode was less than 2 hours, which was much faster compared to other machining methods. The sealing of the reservoir along with the electrical insulation was assured by the self-fusing silicone and Kapton electrical insulating tapes. The laser machineable self-fusing silicone can naturally bound with both silica wafers and conductive silicone sheets when heated under 300 °F for 30 min, forming a perfect sealing medium between the holder of the emitter and the distributor. Meanwhile, Kapton tapes between the extractor and the distributor play two roles on the emitter: electrical insulators at high voltages and spacer for controlling the gap between the tip of the nozzle and the slot on the extractor.

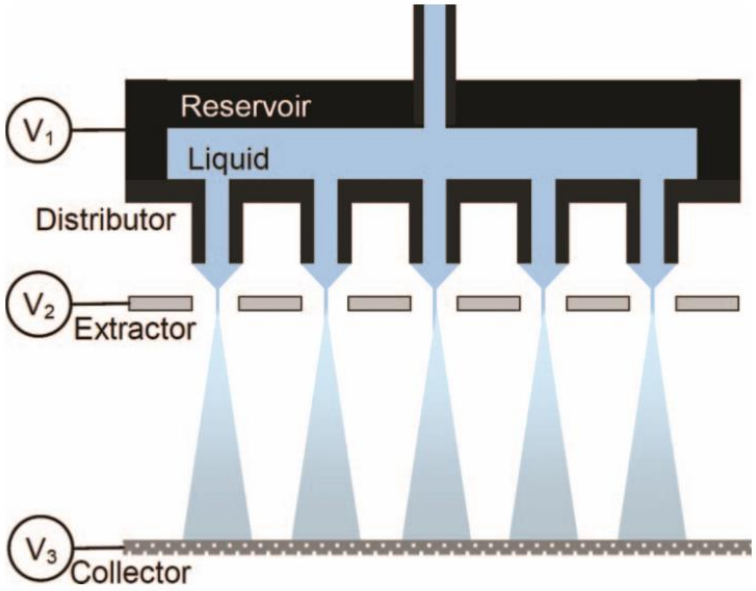

Figure 30: Diagram for the typical three-electrode MES emitter[11]

4.1 Design of Electrodes

Three-electrode configuration was successfully implemented to enable the operation of cone-jet mode at a relatively high nozzle packing density. These three electrodes (distributor, extractor, and collector) were designed to separate the domain into two electric fields: the cone-jet forming region and the spray forming region. The cone-jet forming region is the space between the distributor and the extractor, and the nozzle-extractor gap was comparable to the outer diameter of the capillary. Within this region, the conical liquid will form at the tip of the capillary and jets extending from the cone will break up before or shortly after passing through the slot on the extractor. The spray-forming region provides sufficient driving force for charged droplets to guide them onto the collector. The magnitude of electric fields in both regions can be controlled by adjusting the voltages applied to electrodes.

Typically, electrodes can be connected in two different ways. Power supplies with opposite polarity can be connected to the distributor and the collector while the extractor will be grounded. This configuration enables us to control the cone-jet forming region and spray forming region separately by changing the potential of the power supply connected to the distributor or the collector. Alternatively, high voltage power supplies with the same polarity can also be separately connected to the distributor and the extractor while the collector will be grounded. In this way, both power supplies need to be adjusted in order to only change the electric field in the spray-forming region. We used the second electric connection strategy to simplify the electrical connection.

4.1.1 Distributor

The distributor is the electrode that contains nozzle arrays that can evenly distribute the liquid to the tip of nozzles. All distributors were machined on the 1.5 mm thick silicone sheet. A single nozzle has three main parameters: inner diameter, outer diameter, and the height. For the nozzle arrays, the number of nozzles and their arranging pattern were two additional parameters that could be convieiently changed through the GUI. We chose the nozzle to be cylindrical as in most recent publications although the rectangular cross-section was also reported[34]. Figure 31 (b) shows the SEM image of a laser machined nozzle tilted 45° with

respect to the surface normal. The nozzle was 300 μm in the outer diameter, 55 μm in the inner diameter and 600 μm in height.

The minimum outer diameter of the nozzle tested was 150 μm as shown in Figure 32 (a). Taking advantage of a flexible tool path adjustment capability of the fiber laser marker system, the layout of the nozzle array can be easily adjusted into linear, circular, hexagonal, or other repeating pattern. Regardless of the array layout, we need to keep the electric field nearly identical for each nozzle by carefully aligning the corresponding extractor with the nozzle array. However, linear or planar nozzle array requires extra dummy nozzles to weaken the "edge effect". For nozzle array configurations without close loops of nozzles, the nozzle left at the edge only has one neighboring nozzle, which results in an asymmetric electric field. Thus, dummy nozzles (without though holes) are added at the end of each nozzle array to offset the edge effect. The existence of the dummy nozzle can be observed in Figure 32(a).

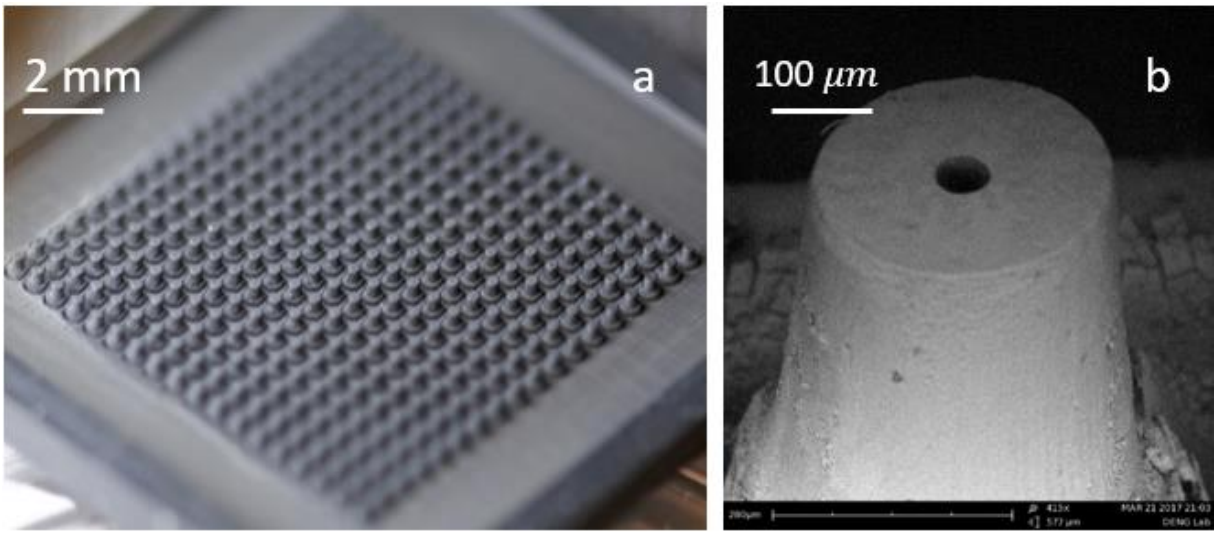

Figure 31: (a) 16×16 square nozzle array surrounded by dummy nozzles: (b) SEM scan of a single nozzle. Image was taken at 45° angle with respect to the surface normal

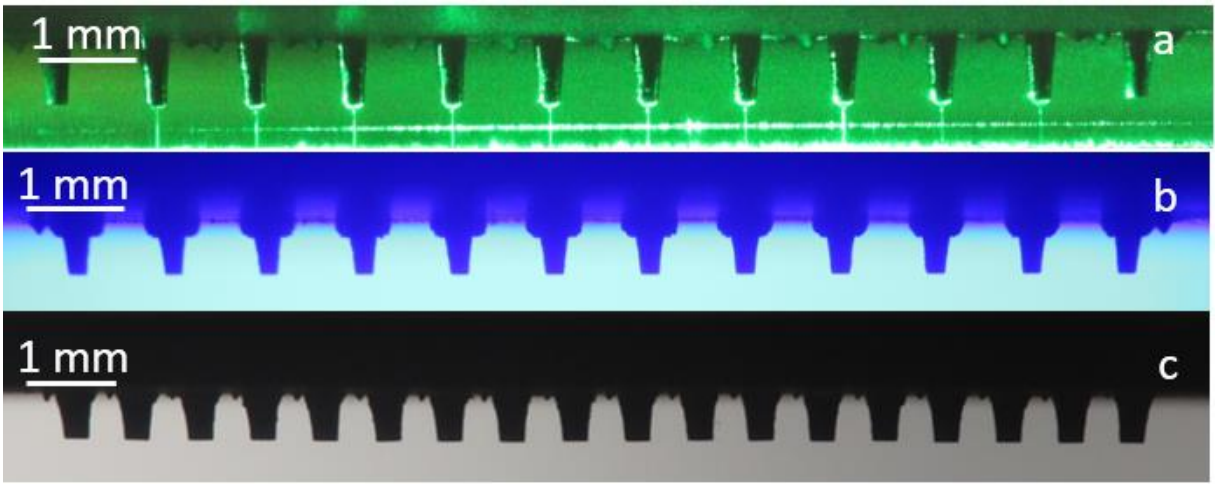

Figure 32 ： 12×1 linear nozzle array with (a) 150 µm OD, 1mm pitch; (b) 175 µm OD, 1 mm pitch; (c) 16×1 linear nozzle array with 300 µm OD, 0.75 mm pitch

4.1.2 Extractor

The extractor is an electrode positioned between the distributor and the collector to prevent the cone-jet from being influenced by the space charge created by sprays. The extractor is a stainless steel sheet with laser machined opening which will be aligned to the nozzle array. The opening on the extractor can be through holes under each corresponding nozzle or simply a slot. Either through holes or slot allow droplets to pass through the cone-jet forming region and break up into finer droplets immediately in spray region. For convenient alignment and observation, a slot with 500µm width was chosen as shown in Figure 33. This design is also less prone to flooding while providing sufficient electric field isolation.

Figure 33: Extractor machined on stainless steel with a 500 µm slot

4.1.3 Collector

The collector is the grounded electrode positioned below the extractor to provide sufficient driving field strength (a few kV/cm) to overcome the space charge. In order to prevent the liquid accumulation, the metal mesh was used as the collector under high flow rate up to $1.6\ ml/h/nozzle$. Spray uniformity and jets' diameter measurement shown in the following chapter were both carried out with this collector geometry. For perovskite solutions deposited under the flow rate of 4 nl/s/nozzle, FTO glass covered with the pre-coated TiO_2 film will be used as the collector.

4.2 System Integration

The silicone based multiplexed electrospray system consists of five components: fused silica holder, reservoir layer, distributor, extractor, and collector. Except for the collector, the other four components need to be integrated together as an entirety with perfect liquid sealing and electrical insulation.

4.2.1 Reservoir sealing

Before utilizing the self-fusing silicone as the reservoir layer material, several sealing methods such as glues, double sided tapes, and clamps were tested, but all failed due to poor adhesion or low durability. Self-fusing silicone will not only bond itself into a strong and electrically insulating layer but can also firmly bond with fused silica, 1.5 mm thick silicone sheet and 750 μm thick silicon wafer when heated to 300 °F for 30 min. Thus, the self-fusing silicone can be used for sealing the reservoir machined on the back of conductive silicone sheet as well as bonding with either fused silica or silicon wafer as the holder of the whole system. Meanwhile, the 0.5 mm thick self-fusing silicone is laser machinable. Thus one alternative reservoir sealing strategy was to directly cut "L" shaped reservoir on the self-fusing silicone sheet and bond it with fused silica. Beside good sealing capability and high durability, another exclusive advantage for this design is that the transparent fused silica holder enabled us to monitor the liquid flow inside the reservoir during the experiment. Another reservoir configuration was to utilize the microfluidic channel machined on the silicon wafer to provide

individual liquid supply for each nozzle. The sealing strategy for this reservoir configuration was similar to the common reservoir and the self-fusing silicone sheet was still used as the sealing medium but also as a liquid transportation layer.

4.2.2 Electrical connection and insulation

Removable yet secure electrical connections were made at the distributor, extractor, and collector. Here, we grounded the collector and connected the distributor and the extractor to high voltage power supplies. The extractor was inserted into a flat aluminum socket soldered with the high voltage cable. The clamp was 5 mm in depth with the same width as the extractor. As for the distributor, all components directly or indirectly contacted with the distributor including the distributor itself were nonmetal materials. The only conductive part was the silicone distributor with only 0.9 mm in thickness after the laser milling, which means ordinary electrical connection methods such as soldering, clamping or threading were not applicable. A needle convolved with high voltage wires was inserted into the distributor from the side. The needle and the wire were surrounded by a few layers of 127 μm thick Kapton tape as an electrical insulation layer. The voltage applied on the distributor is lower than 5000 V while a single layer of this Kapton tape was guaranteed to withstand 7000 V.

Electrical insulation between the distributor and extractor is critical for the successful operation of the MES system. Meanwhile, the space between the tip of the nozzle and the slot of the extractor was also controlled by the electric insulation layer between the distributor and the extractor. Key ingredients involved were three types of Kapton tapes: 60 μm thick Kapton polyimide masking tape, 127 μm and 254 μm thick Kapton electrical tape with adhesives on both sides. The combination of these three tapes along with the precision milling process enables well-controlled gap. Noticing that a single layer of 127 μm or 254 μm thick Kapton tape can withstand 7000 V or 17000 V thus the electrical insulation is relatively easy to accomplish in this design.

4.2.3 Liquid supply

4.2.3.1 Common reservoir

The liquid was supplied by inserting a needle with 300 μm OD and 150 μm ID into the reservoir from the short end of the "L" shaped common reservoir. A syringe pump was connected to the needle using the Teflon tube which was also anti-corrosion. By utilizing the sealing method mentioned above, the reservoir had already been well sealed before integrating the liquid supply needle onto the system. Thus, the needle was directly inserted into the common reservoir through the silicone distributor.

4.2.3.2 Individual microfluidic channels

For individual microfluidic channels, the liquid at each branch was supplied by the previous branch. Thus, 16 individual channels gradually converged into a common channel with 80 μm in width and 30 μm in depth. By drilling a through hole with 1 mm in diameter on the silicon wafer, a Teflon tube was inserted from the back of the silicon wafer. The tube was then sealed by the super glue.

CHAPTER 5: MES emitters operation

In this chapter, the prerequisite for the strength of the electric field between the extractor and the collector was calculated. Such driving field must overcome the space charge field generated by sprays to prevent droplets from flying back to the extractor. With this estimation, linear nozzle arrays with different nozzle array and nozzle configurations were tested. The profile of the spray was visualized by using a 532 nm laser sheet along the direction of the linear nozzle array while the stability of Tayler cones was monitor by using a red LED light source forming a shadowgraph configuration. Images of 10×1 linear nozzle arrays (P=1mm, ID=55 μm, L=600 μm) and 16×1 linear nozzle arrays (P=0.75mm, ID=55 μm, L=600 μm) tested with ethanol under high flow rate (0.6 ml/h/nozzle ~ 1.6ml/h/nozzle) were shown in section 4.2. The flow rate uniformity was then examined by measuring the jet diameter. The result indicated that there was approximately 20 percent variation in the flow rate for current MES emitters.

5.1 Estimation of critical field

Within the spray-forming region between the extractor and the collector, the intense space charge of the dense spray of charged droplets would generate the repulsive field that may drive the droplet back to the extractor and eventually flood the extractor. As discussed in the previous section, the extractor was used as the barrier between the cone-jet region and the spray-forming region so that two independent electric fields could be formed between electrodes. However, the potential applied between the extractor and the collector need to exceed a critical value so that droplets would get sufficient acceleration toward the collector. This critical value E_c was determined by the largest space charge electric field. For a single electrospray, the strongest space charge appears right beneath the extractor where jets break up into droplets. For multiplexed electrospray profile, space charge is most intense at the center of the nozzle array. The work by Lojewski [11] provides us the following method to estimate the upper limit of this critical field [11]:

$$E_c = \sum_{i=1}^{(N-1)/2} E_{c,i} < \sum_{i=1}^{(N-1)/2} E_{ref} \frac{1}{i} \approx E_{ref} \ln\left(\frac{N}{2}\right) = \frac{\lambda}{\pi \varepsilon_0 P_0} \ln\left(\frac{N}{2}\right)$$

where i is the i^{th} pare of nozzles relative to the center of the nozzle array, λ is the line charge density defined by $\lambda = I_0/v_z$. I_0 is the average current of each nozzle. When stably spraying pure ethanol, I_0 is approximately $7\ nA$. v_z is the velocity of the droplet vertical to the extractor which is ~$10\ \mathrm{m/s}$. ε_0 is the vacuum permittivity ($8.9\ \mathrm{pF/m}$). P_0 is the pitch between each nozzle, N is the total number of nozzles on the emitter. For the 16×1 linear nozzle array shown in Figure 32 (c), $P_0 = 0.75mm$ and $N = 16$, we find $E_c = 694\ V/cm$. Thus, when spraying pure ethanol, the minimum driving field between the extractor and the collector is $694\ V/cm$ in order to prevent droplets from flying back to the extractor. When spraying fluids with higher conductivity or higher flow rates, or both, the minimum driving field will be higher. For instance, when the conductivity of the liquid increased to$1.4\ \mu\mathrm{S/cm}$, the average current of each nozzle increased from $7\ nA$ to $13\ nA$, yields $E_c = 1.29\ kV/cm$ .Correspondingly, the minimum driving field required between the extractor and the collector increased to $1.29\ kV/cm$.

5.2 Spray profile

In order to monitor the operation of the MES emitter, two types of light sources were applied to the experiment set up. The red LED light source positioned parallel the axis of the camera lens was used to observe the stability of the Taylor cone inside the cone-jet region. Generally, with a fixed conductivity of the liquid, Taylor cones were relatively easier to stabilize under high flow rate. The spray profile of the MES emitter was then visualized by a 532 nm green laser source. The laser beam was converted into a laser sheet by adding a cylindrical lens right after the laser was generated. When the laser sheet was positioned through the center line of sprays, the spray profile could be captured. Nozzles with 150 μm OD were tested and successfully generated ten stable cones (Figure 34 (a)). Even though silicone nozzle would not be easily ruptured by external forces, nozzles with 150 μm OD could not survive the post-cleaning process without been bent. Such deformation increased the risk of the flooding. Thus, we adjusted the OD of the nozzle to 175 μm and increased the nozzle base diameter for each

nozzle to reinforce the nozzle structure during the post-cleaning process. Figure 34 (b) shows the configuration of the array consists of nozzles with 175 μm OD. However, in order to decrease the flow resistance needed to evenly distribute the liquid when spraying highly conductive liquid, the outer diameter of the nozzle was increased to 300 μm so that the surface tension pressure would be decreased by 50% compared to the nozzle with 150 μm OD. The spray profile of a 16×1 nozzle array consists of such nozzles is shown in Figure 34 (e).

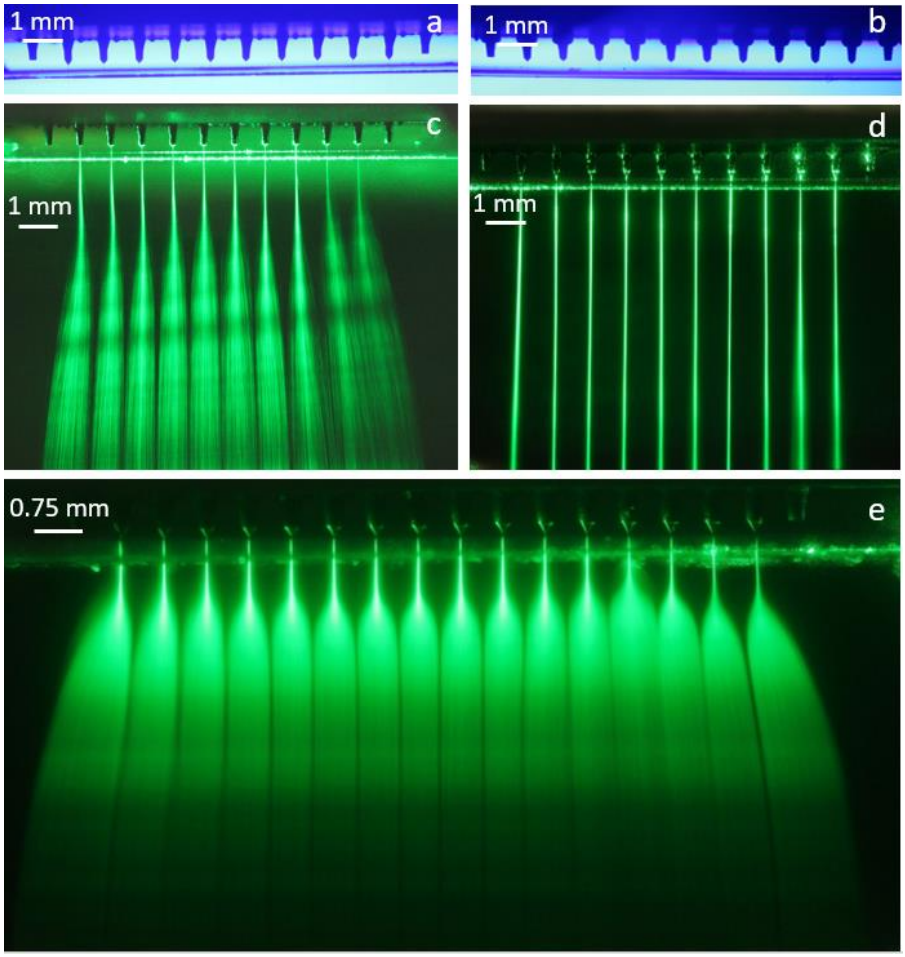

Figure 34：Nozzle array with ID=55, OD=150, P=1mm, N=10: (a) stable cone jets, (c)spray profiles; Nozzle array with ID=55, OD=175, P=1mm, N=10: (a) stable cone jets, (b)spray profiles; (e)spray profiles of a nozzle array with ID=55, OD=150, P=1mm, N=16

5.3 Flow rate uniformity

The uniformity of the flow rate was an indicator of the uniformity of the flow resistance provided by the flow-resistive channels. Checking the uniformity of the flow resistance between each nozzle was another method to verify the uniformity of the through hole diameter other than the brutal method introduced in Section 3.1.5. Assuming cone jets had same speed under the same driving field, the flow rate would be proportional to the square of the jet diameter. Thus, we mounted a microscope that provided sufficient resolution of $0.5\ \mu m/pixel$ to quantify the diameter of the cone jet emitted from each nozzle. The 16×1 nozzle array with $P = 0.75\ mm, ID = 55\ \mu m, OD = 300\ \mu m, L = 600\ \mu m$ was then tested with the diluted ethanol-water solution. The conductivity of the solution was extremely low, which would prevent the breakup of the jet from influencing the accuracy of the measurement. Figure 35 shows images of 16 nozzles with cone-jet mode along with two dummy nozzles at both ends of the nozzle array, from which we measured the diameter of jets. Three average flow rates were used on the emitter:$0.8,1.2\ and\ 1.6ml/h/nozzle$. The diameter of the cone jet would decrease as the liquid approaching the extractor within the cone-jet region. Thus, all data points were measured right above the extractor. The result shown in Figure 36 indicated that the distribution of the liquid followed a similar distribution under different total flow rate. Table 9 summarized the average diameter of cone jets and the standard deviation. There was around 10% variation in cone jets' diameter, which means the individual flow rate of each nozzle has up to 20% variation. A similar process was applied to several nozzle arrays with different inner diameters, the result of which drew the same conclusion.

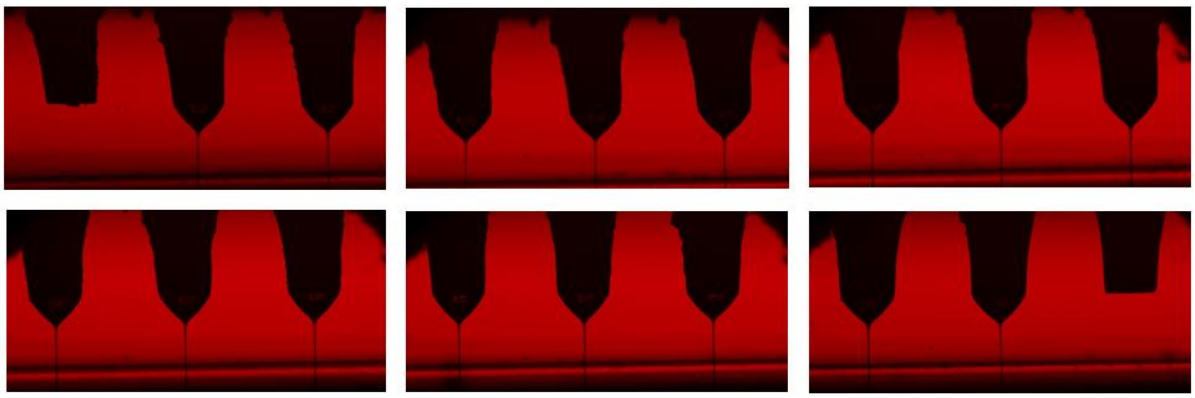

Figure 35: Stable cone jets of a 16×1 nozzle array under Q=1.2ml/h/nozzle

Table 9: Diameter uniformity of jets right above the extractor

Flow rate	0.8ml/h/nozzle	1.2ml/h/nozzle	1.6ml/h/nozzle
Average jets diameter / $\boldsymbol{\mu m}$	9.6	10.8	13.1
STDVE of jets diameter / $\boldsymbol{\mu m}$	0.86	1.10	1.14
Variation	8.9%	10.1%	8.7%

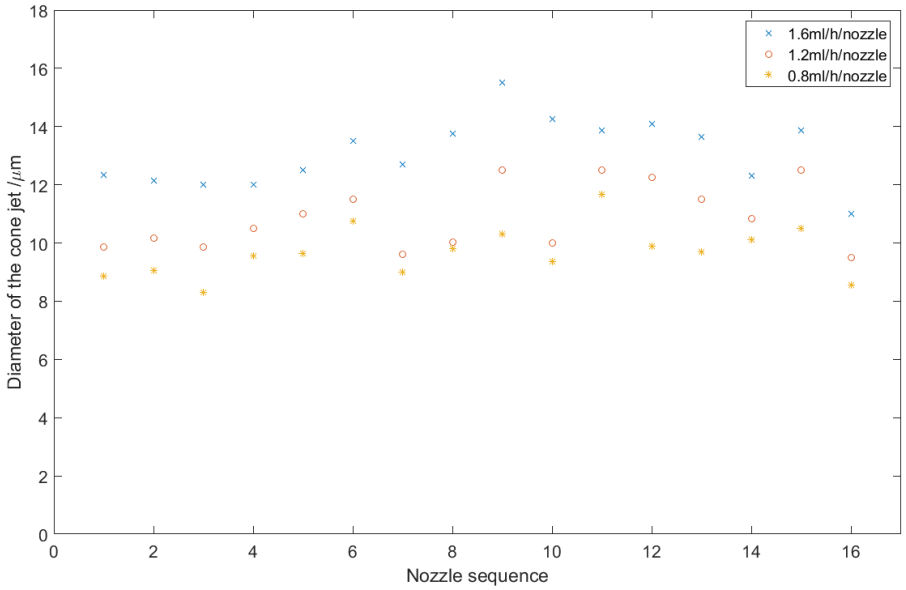

Figure 36: The cone-jet diameter of a 16×1 nozzle array under different flow rate

CHAPTER 6: CONCLUSIONS

This thesis reports the design, fabrication, and operation of silicone based multiplexed electrospray (MES) emitters.

We first present a design rationale for MES suitable for highly conductive and corrosive fluids. Then we customized a 1064nm fiber laser micromachining system to precisely and rapidly machine silicone sheet and silicon wafers. Judiciously chosen laser energy and path are chosen to create clean and round micro posts that form the external structure of the nozzles. To make the pressure drop inside each fluid flow channel overcome the surface tension, we modeled the dimension of microfluidic.

Next, we presented laser microfabrication techniques for fabricating two typical types of microfluidic channels: the through-hole array on conductive silicone sheets and the in-plane microfluidic channel on silicon wafers. Decent uniformity of the flow rate (RSD=20%) among nozzles on MES emitters. The results suggest that the laser micromachining method strikes a good balance among precision, speed, convenience, and cost. As a versatile machine tool, the laser system is fully capable of handling micro drilling, milling, and engraving tasks on multiple materials including silicone, silicon, and aluminum. Uniformed silicone nozzle arrays with various configurations were successfully machined and integrated on MES emitters.

This thesis also addressed two major challenges for electrospraying liquid solutions of perovskite precursors, which require the MES emitter to be anti-corrosion and operating under relatively low flow rates. We designed a three-electrode emitter array and fabricated flow resistive channels that were able to provide sufficient pressure drop under the extremely low flow rate ($4\ \mathrm{nl/s/nozzle}$). The design of MES emitters in this thesis can process highly corrosive fluids because the components that directly contact with the liquid on the MES emitter are made in silica, silicon or silicone. The experiment result suggest that silicone-based MES emitters we developed in this thesis are feasible for spraying highly conductive and corrosive liquids.

LIST OF REFERENCES

1. Prunet-Foch, M.C.B., *Electrohydrodynamic spraying functioning modes: a critical review.* Journal of Aerosol Science, 1994.
2. Taylor, G., *Disintegration of water drops in an electric field.* Sciences, 1964.
3. Deng, W., et al., *Compact multiplexing of monodisperse electrosprays.* Journal of Aerosol Science, 2009. **40**(10): p. 907-918.
4. Rulison, A.J. and R.C. Flagan, *Scale‐up of electrospray atomization using linear arrays of Taylor cones.* Review of Scientific Instruments, 1993. **64**(3): p. 683-686.
5. Shun-Chi Chang, J.L., Jayesh Bharathan, Yang Yang,* JunOnohara and Junji Kido, *Multicolor Organic Light-Emitting Diodes Processed by Hybrid Inkjet Printing.* 1999.
6. Shaheen, S.E., et al., *Fabrication of bulk heterojunction plastic solar cells by screen printing.* Applied Physics Letters, 2001. **79**(18): p. 2996-2998.
7. Schilinsky, P., C. Waldauf, and C.J. Brabec, *Performance Analysis of Printed Bulk Heterojunction Solar Cells.* Advanced Functional Materials, 2006. **16**(13): p. 1669-1672.
8. Green, R., et al., *Performance of bulk heterojunction photovoltaic devices prepared by airbrush spray deposition.* Applied Physics Letters, 2008. **92**(3): p. 033301.
9. Kelly, R.T., *Capillary-Based Multi Nanoelectrospray Emitters: Improvements in Ion Transmission Efficiency and Implementation with Capillary Reversed-Phase LC-ESI-MS.* A n a l y t i c a l C h e m i s t r y 2008.
10. Grustan-Gutierrez, E. and M. Gamero-Castaño, *Microfabricated Electrospray Thruster Array with High Hydraulic Resistance Channels.* Journal of Propulsion and Power, 2017: p. 1-8.
11. Lojewski, B., et al., *Design, Fabrication, and Characterization of Linear Multiplexed Electrospray Atomizers Micro-Machined from Metal and Polymers.* Aerosol Science and Technology, 2013. **47**(2): p. 146-152.
12. Hill, F.A., et al., *High-Throughput Ionic Liquid Ion Sources Using Arrays of Microfabricated Electrospray Emitters With Integrated Extractor Grid and Carbon Nanotube Flow Control Structures.* Journal of Microelectromechanical Systems, 2014. **23**(5): p. 1237-1248.
13. https://www.ossila.com/pages/perovskites-and-perovskite-solar-cells-an-introduction
14. A. Kojima, K.T., Y. Shirai, and T. Miyasaka, *Organometal Halide Perovskites as Visible-Light Sensitizers for Photovoltaic CellsOrganometal Halide Perovskites as Visible-Light Sensitizers for Photovoltaic Cells.* J. Am. Chem. Soc, 2009.
15. McGehee, M., *Materials science: Fast-track solar cells.* Nature, 2013.
16. B. O'Regan, a.M.G., *A low-cost, high-efficiency solar cell based on dye-sensitized colloidal TiO2 films.* Nature, 1991.
17. Liu, M., M.B. Johnston, and H.J. Snaith, *Efficient planar heterojunction perovskite solar cells by vapour deposition.* Nature, 2013. **501**(7467): p. 395-8.
18. M. M. Lee, J.T., T. Miyasaka, T. N. Murakami, and H. J. Snaith, *Efficient Hybrid Solar Cells Based on Meso-Superstructured Organometal Halide Perovskites.* Science, 2012.
19. Heeger, A.J., *Semiconducting polymers: the Third Generation.* Chem Soc Rev, 2010. **39**(7): p. 2354-71.
20. Burschka, J., et al., *Sequential deposition as a route to high-performance perovskite-sensitized solar cells.* Nature, 2013. **499**(7458): p. 316-9.
21. Im, J.H., et al., *6.5% efficient perovskite quantum-dot-sensitized solar cell.* Nanoscale, 2011. **3**(10): p. 4088-93.

22. Shrotriya, V., et al., *Absorption spectra modification in poly(3-hexylthiophene):methanofullerene blend thin films.* Chemical Physics Letters, 2005. **411**(1-3): p. 138-143.
23. C. C. Stoumpos, C.D.M., and M. G. Kanatzidis, *Semiconducting Tin and Lead Iodide Perovskites with Organic Cations: Phase Transitions, High Mobilities, and Near-Infrared Photoluminescent Properties.* Inorg. Chem., 2013.
24. D. Stranks, G.E.E., G. Grancini, C. Menelaou, M. J. P. Alcocer, T. Leijtens, L. M. Herz, A. Petrozza, and H. J. Snaith, *Electron-Hole Diffusion Lengths Exceeding 1 Micrometer in an Organometal Trihalide Perovskite Absorber.* Science, 2013.
25. G. Xing, N.M., S. Sun, S. Lim, Y. Lam, M. Grätzel, S. Mhaisalkar, and T. C. Sum, *Long-Range Balanced Electron- and Hole-Transport Lengths in Organic-Inorganic CH3NH3PbI3.* Science, 2013.
26. J. You, Z.H., Y. (Michael) Yang, Q. Chen, M. Cai, T. B. Song, C.-C. Chen, S. Lu, Y. Liu, H. Zhou, and Y. Yang, *Low-Temperature Solution-Processed Perovskite Solar Cells with High Efficiency and Flexibility.* ACS Nano, 2014.
27. Cacciari, M., M.L. Mangano, and P. Nason, *Gluon PDF constraints from the ratio of forward heavy-quark production at the LHC at [Formula: see text] and 13 TeV.* Eur Phys J C Part Fields, 2015. **75**: p. 610.
28. Maiman, T.H., *Stimulated Optical Radiation in Ruby.* Nature, 1960. **187**(4736): p. 493-494.
29. *Introduction*, in *Fiber Lasers*. 2016, CRC Press. p. 1-8.
30. Campanelli, S.L., et al., *Experimental analysis of the laser milling process parameters.* Journal of Materials Processing Technology, 2007. **191**(1-3): p. 220-223.
31. Leone, C., et al., *Experimental investigation on laser milling of aluminium oxide using a 30W Q-switched Yb:YAG fiber laser.* Optics & Laser Technology, 2016. **76**: p. 127-137.
32. Dubey, A.K. and V. Yadava, *Experimental study of Nd:YAG laser beam machining—An overview.* Journal of Materials Processing Technology, 2008. **195**(1-3): p. 15-26.
33. Wang, C.-J., et al., *Effect of Laser Power on the Quality of Drilled Micro Hole Using Cu50Zr50 Amorphous Alloys Foils.* Micromachines, 2014. **5**(4): p. 1061-1068.
34. Woong Kim , M.G., Peidong Yang ,and Daojing Wang *Microfabricated Monolithic Multinozzle Emitters for Nanoelectrospray Mass Spectrometry.* Anal. Chem pp 3703–3707, 2007.